

### Discerning the duality of H in Mg H-induced damage and ductility

Ji, Yucheng; Shuang, Fei; Ni, Zhiyang; Yao, Chenyang; Li, Xiao; Fu, Xiaoqian; Chen, Zhanghua; Li, Xiaogang; Dong, Chaofang

10.1016/j.ijplas.2024.104084

**Publication date** 2024

**Document Version** Final published version

Published in International Journal of Plasticity

Citation (APA)

Ji, Y., Shuang, F., Ni, Z., Yao, C., Li, X., Fu, X., Chen, Z., Li, X., & Dong, C. (2024). Discerning the duality of H in Mg: H-induced damage and ductility. International Journal of Plasticity, 181, Article 104084. https://doi.org/10.1016/j.ijplas.2024.104084

Important note

To cite this publication, please use the final published version (if applicable). Please check the document version above.

Other than for strictly personal use, it is not permitted to download, forward or distribute the text or part of it, without the consent of the author(s) and/or copyright holder(s), unless the work is under an open content license such as Creative Commons.

Takedown policy
Please contact us and provide details if you believe this document breaches copyrights. We will remove access to the work immediately and investigate your claim.

## Green Open Access added to TU Delft Institutional Repository 'You share, we take care!' - Taverne project

https://www.openaccess.nl/en/you-share-we-take-care

Otherwise as indicated in the copyright section: the publisher is the copyright holder of this work and the author uses the Dutch legislation to make this work public.

ELSEVIER

Contents lists available at ScienceDirect

#### International Journal of Plasticity

journal homepage: www.elsevier.com/locate/ijplas



## Discerning the duality of H in Mg: H-induced damage and ductility



Yucheng Ji <sup>a,b</sup>, Fei Shuang <sup>c</sup>, Zhiyang Ni <sup>d</sup>, Chenyang Yao <sup>a</sup>, Xiao Li <sup>d</sup>, Xiaoqian Fu <sup>a</sup>, Zhanghua Chen <sup>d</sup>, Xiaogang Li <sup>a</sup>, Chaofang Dong <sup>a, \*</sup>

- <sup>a</sup> Beijing Advanced Innovation Center for Materials Genome Engineering, National Materials Corrosion and Protection Data Center, Institute for Advanced Materials and Technology, University of Science and Technology Beijing, Beijing 100083, China
- b School of Computer and Communication Engineering, University of Science and Technology Beijing, Beijing 100083, China
- c Department of Materials Science and Engineering, Mechanical Engineering, Delft University of Technology, Delft 2628CD, the Netherlands
- <sup>d</sup> School of Mathematics and Physics, University of Science and Technology Beijing, Beijing 100083, China

#### ARTICLE INFO

# Keywords: Magnesium Hydrogen-induced ductility Cracking Twining Multi-scale calculation

#### ABSTRACT

Prone H reduction is considered an important factor in the poor corrosion resistance of Mg and its alloys, while the reduced H simultaneously impacts their mechanical properties whose mechanism is still unclear. It can be experimentally found that the elongation of Mg charged with atomic H is 2.76 % greater than that in air. To reveal the underlying physics, multi-scale modeling combining first-principle calculation, molecular dynamic/static (MD/MS) simulation, and crystal plasticity finite element method (CPFEM) is first employed to elaborate the influence of H on Mg at different length scales. The first-principle results show that the Prism-I  $\{10\overline{1}0\}$  exhibits the most corrosive nature with an effective H adsorption density that reaches 18 nm<sup>-2</sup> and its diffusion barrier is only 0.156 eV  $H^{-1}$ . Conversely, the Basal {0001} has the best surficial H resistance. After H infiltration into the Mg matrix, the generalized stacking fault energies of most twining planes decrease by 2.26 % ~18.49 %. Especially for the Basal {0001}, the H not only lowers its stacking fault energy to -7.13 J  $m^{-2}$ , but also impedes its cleavage cracking along  $[10\overline{1}0]$  according to the MD/MS simulation. The presence of H within the grains induces early initiation of stacking fault and elevates the critical stress at the crack tips. The CPFEM modeling reveals that the difference in twining growth is concentrated within 4 % strain. The H addition promotes the twining of Mg, however, following 4 % strain, the relative activity of planes in the Mg/Mg-H models is consistent.

#### 1. Introduction

As the lightest metals used in engineering, Mg alloys are applied in the biomedical sectors, automotive, and aerospace industries (Liu et al., 2018; Tsakiris et al., 2021). Their inferior corrosion resistance and mechanical properties limit their further applications. Conventionally, the reason for Mg corrosion is attributed to its high negative potential, which makes its surface prone to reducing  $H^+$  to H atoms. Even though oxide films (MgO) form on the surface, their soluble nature and the electrochemical circuit promote the transformation of Mg atoms to Mg<sup>2+</sup>(Wang et al., 2020). Thus, corrosion-resistant designs for Mg alloys are difficult (Man et al., 2020; Yan et al., 2021). Decreasing or blocking the H reduction on the Mg surface seems to be a feasible method, such as overcoating (Calado et al., 2020; Wei et al., 2020) or adding corrosion inhibitors (Lee et al., 2019; Zhao et al., 2018). Few studies have been conducted to

E-mail address: cfdong@ustb.edu.cn (C. Dong).

https://doi.org/10.1016/j.ijplas.2024.104084

<sup>\*</sup> Corresponding author.

improve the intrinsic corrosion resistance of Mg alloys by alloying or creating new phases (Wang et al., 2022). However, these phases were mainly designed for mechanical improvements, and some of them resulted in the occurrence of galvanic corrosion or pitting. To prevent H reduction and reduce the hazard of corrosion, much research has attempted to adjust the composition of Mg alloys by tailoring the Zn, Li, or Y content (He et al., 2020; Thekkepat et al., 2021). As indicated in these studies, H is an important factor in Mg corrosion and corrosion resistance design.

In terms of mechanical properties, H atoms are generally considered a source of serial damages, such as hydrogen embrittlement (HE) and hydrogen-induced ductility loss, especially in steel and Al alloys (Cotterill, 1961; Ji et al., 2019). However, the mechanism of HE is complex, its relationship with the materials, dislocations, and loading conditions is still under investigation (Singh et al., 2022; Sun et al., 2021). The contribution of H to materials can be identified as hydrogen-enhance local plasticity (HELP) and hydrogen-enhanced decohesion (HEDE) (Chen et al., 2024). For instance, Ogawa group (Nishida et al., 2022; Ogawa et al., 2020) used H to stabilize austenitic stainless steel enhancing the strength and ductility of steel, the prominent ductility was attributed to the twin nucleation accelerated by H-dislocation interaction. Besides, the effects of H-charging methods on the ductility of transformation-induced plasticity steel are discussed (Depover et al., 2020), the results showed that electrochemically charged H caused a decrease in plasticity, whereas H charged with plasma prevented crack initiation.

So far, the mechanism of H action on the Mg mechanical properties in various environments is still under discussion. When the Mg alloy was deformed in the H atmosphere, its elongation increased by  $23.3\,\%$  compared with that in the air (Michler, 2010). Comparing the nominal stress-strain curves of Mg with 35 ppm and 16 ppm H also confirmed that the ductility of samples with more H improved (Chino et al., 2011). Surface H treatment indeed promoted the microstructure evolution of Mg alloys, and then improved their corrosion resistance (Wu et al., 2021). Conversely, Liu et al. (2017) quantitatively calibrated the H content in Mg and found the ultimate tensile strength (UTS) of the AZ91 Mg alloy was improved after dehydrogenation. Besides, Kamilyan et al. (2017) utilized thermal desorption analysis to study H distribution traps in AZ31 Mg alloys, and the subsequent results showed that the dehydriding of the  $\beta$ -phase affected the embrittlement behavior. Further, Ajito et al. (2023) reported that the degradation of AZ31 alloy with cathodic potential became more severe compared to that in air.

This H-induced phenomenon had a clear theoretical discussion in Al (Xie et al., 2021) and steel (Kumar et al., 2023), but not in Mg. The interaction between H/O atoms and different twins is still a critical issue that remains to be solved (Yue et al., 2023). Due to the reaction nature with H ions, the plastic deformation discussion of Mg mainly focused on the twining mechanisms. For instance, the early formation of  $\{10\overline{1}2\}$  twin needed transformation prismatic-to-basal and basal-to-prismatic that simulated by finite element method and molecular dynamic (Jiang et al., 2022). Moreover, the nucleation of  $\{10\overline{1}1\}$  twin was related to the cross-slip of prismatic dislocation (Li et al., 2022). Furthermore, some twins, such as  $\{11\overline{2}6\}$ , was found under special deformation (Gao et al., 2023). If the relationship of dislocation/twining emission in Mg with H atoms can be discussed further, the elucidated H contradictory effect (damage or ductility) will be beneficial for the improvement of corrosion resistance, mechanical properties, and processing of Mg alloys.

In this study, the effects of H atoms on the corrosion behavior and mechanical properties of Mg were investigated through experiments and calculations. Initially, we studied the ductility of Mg alloys with H charging. Its role in the destruction and plasticity of Mg alloys was discussed by comparing fracture and twins. Subsequently, the DFT calculations were performed to discuss the adsorption of H on Mg surfaces ( $\{0001\}$ ,  $\{10\overline{1}1\}$ , and  $\{10\overline{1}0\}$ ). Transition state search (TSS) calculations were utilized to determine the H diffusion barrier from the surface to the matrix. Then, the mechanical elastic stiffness of crystals with different orientations and H atoms was calculated to explain the role of H in the elastic stage. As for the plastic stage, the generalized stacking fault (SF) energy and crack propagation were simulated to elaborate the mechanism for ductility enhancement. Finally, the effect of H in polycrystal Mg was also discussed. These findings can deepen our understanding of H effects on alloys, such as stress corrosion cracking (SCC), and provide guidelines for the design of advanced H-resistance Mg alloys.

#### 2. Methodology

#### 2.1. Mechanical properties experiment in H environments

To detect the effect of H on Mg plasticity, slow strain rate tests (SSRT,  $10^{-6}$  s<sup>-1</sup>) of pure Mg were performed, these tests were carried out three times in each environment to ensure repeatability. Different from the normal stress-strain experiment, the extremely low strain rate of SSRT provided sufficient time for H penetration into the Mg matrix, it reflects the combined effect of environment (H) and mechanics (Li et al., 2020). The total length of the SSRT sample was 140.0 mm, while the middle gauge segment was 40.0 mm. The clamping end and thickness were 50.0 mm and 20.0 mm, respectively. Atomic or ionic H was generated by the combination of electrochemical polarization (-1.6 V referenced to a saturated calomel electrode) and solution pH (14, NaOH). Besides, 1 g  $L^{-1}$  Thiourea was added to inhibit atomic H form molecular H<sub>2</sub> (**Supplementary Materials**). To avoid oxidation, the SSRT samples were abraded with 800–3000 grit abrasive paper in ethanol. The grinding direction was 45° relative to the loading direction. After polishing was performed, the samples were rinsed with ethanol dried, and stored in ethanol. The gripping ends of the SSRT samples in the H environment were sealed with silica gel and the gauge section was completely immersed in the solution.

Electron backscatter diffraction (EBSD, Oxford Symmetry, with a spatial resolution of 2 nm) experiments were performed to determine the grain orientations, and the sampling location was close to the fracture surface of deformed samples had completely fractured. A 5000-grit abrasive paper was used in the final step of mechanical grinding, then we used diamond paste ( $\sim$ 0.2  $\mu$ m) to polish the samples. The electrolytic polishing solution was a mixture of 10 % perchloric acid and 90 % ethanol. The cooling medium

was ethanol reached  $-30^{\circ}$ C, and the electropolishing voltage applied was  $\sim 15$  V. After polishing, the EBSD samples were rinsed with ethanol and stored to prevent oxidation.

#### 2.2. Multiscale calculations

The multiscale calculations (Fig. 1) integrated first-principle based on the density functional theory (DFT, VASP 5.4), molecular dynamics/statics (MD/MS, LAMMPS), and crystal plasticity finite element method (CPFEM, ABAQUS). The surficial adsorption/diffusion of H on different Mg orientations was calculated by DFT. After H penetration, its effect on Mg twining was demonstrated by DFT-calculated stacking fault energy. To correlate the three methods, the DFT calculations determine the H-sensitive orientation and stable position in MD/MS models, the FEM models also summarize the DFT energy and experimental data. With MD/MS simulation, the cracking propagation and twining with H atoms were shown quantitatively. In addition, FEM models refer to the micrometer scale, which reflects the plastic deformation between the grains.

#### 2.2.1. DFT calculations

All the adsorption calculations (Fig. 1a) were conducted on 6-layer slabs of Mg {0001}, {1011}, and {1010} with a 15-Å-thick vacuum gap. The general gradient approximation and Perdew-Burke-Ernzerhof methods were utilized (Kresse and Furthmüller, 1996). The energy convergence accuracy was set to  $10^{-5}$  eV  $\mathring{A}^{-1}$ . The spacing of k-points and cutoff energy for adsorption calculation was set to 0.2  $\mathring{A}^{-1}$  and 450 eV, respectively. The surface energy  $\gamma_{surf}$  (Eq. (1)), adsorption energy  $E_{ads}$  (Eq. (2)), and the Gibbs free energy change  $\Delta G_{dis}$  of one Mg dissociated from the surface at 0 K (Eq. (3)) were calculated using the following equation.

$$\gamma_{surf} = \left(E_{surf} - nE_{Mg}\right) / 2A \tag{1}$$

where  $E_{surf}$  represents the DFT total energy,  $E_{Mg}$  indicates the energy of a single Mg atom in the bulk, n and A express the atom number and surface area.

$$E_{ads} = E_{surf}^{H} - E_{surf} - \frac{1}{2} E_{H_2} \tag{2}$$

where  $E_{surf}^H$  is the total energy of the model with one H,  $E_{surf}$  is the pure system without H adsorbed, and  $E_{H2}$  is the energy of H<sub>2</sub>.

$$\Delta G_{dis} = E_0 - E_r - (m E_{Mg} + n E_H) \tag{3}$$

where  $E_0$  and  $E_r$  express the total energy of the system with Mg removed and the perfect model with H adsorbed, respectively; m and n indicate the number of removed Mg and absorbed H.

To determine whether the H atoms diffused easily into the matrix, the diffusion energy barrier was calculated by TSS. For the TSS calculation from surface to bulk, a nudged elastic band was used to map the minimum energy path between the initial and final systems with three intermediate images. The spring constant was  $5 \text{ eV}\text{Å}^{-2}$ , and the TSS stopped when the force per atom in the system was  $<0.02 \text{ eV} \, \text{Å}^{-1}$ . The cutoff energy for the TSS calculation was 450 eV, and the package used was VTST (Sheppard et al., 2012).

The elastic modulus calculation (Eq. (4)) follows Hooke's law, the deformation (stress  $\sigma_{ij}$  and strain  $\varepsilon_{ij}$ ) within the elastic limit is directly proportional to the external force. In addition, these calculations required two conditions which are ignoring the effects of temperature change and shear strain on the total energy and normal strain under small deformation. The total energy E and elastic constant  $\varepsilon_{ij}$  can be expressed as follows.

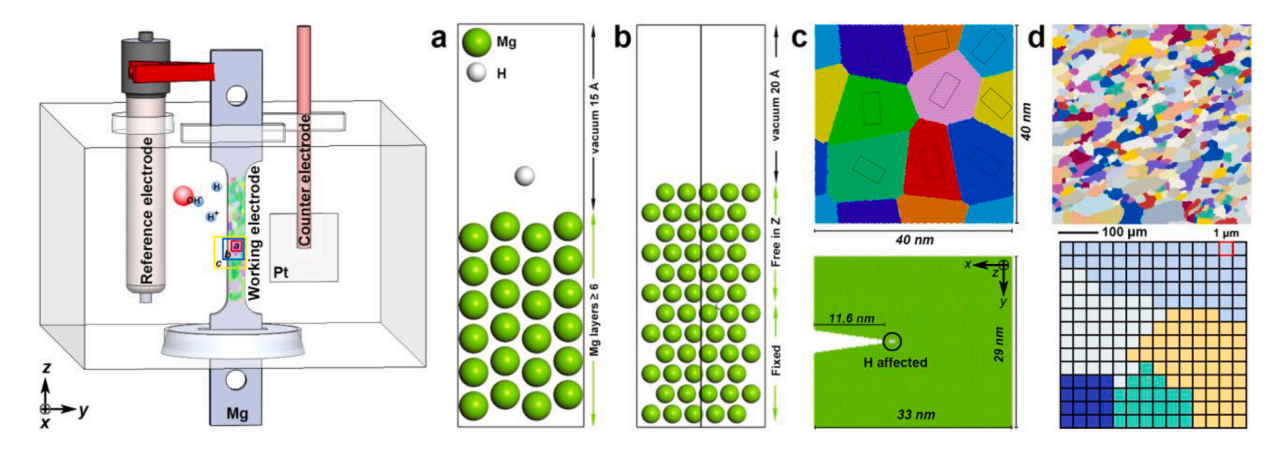


Fig. 1. SSRT of Mg alloys in atomic/ionic H environment and multi-scale calculation models based on (a) DFT: H atom adsorption and diffusion, and (b) stacking fault energy calculation. (c) MD/MS: atomic twining and crack propagation. (d) FEM: polycrystal plastic deformation and its mesh size is the same as EBSD.

$$\{\sigma_{ij}\} = [c_{ij}]\{\varepsilon_{ij}\} \tag{4}$$

$$E = WV ag{5}$$

$$c_{ij} = \frac{\partial W}{\partial \varepsilon_i \partial \varepsilon_j} = \frac{1}{V} \frac{\partial^2 E(V, \varepsilon_k)}{\partial \varepsilon_i \partial \varepsilon_j} \tag{6}$$

where W is the cohesive energy density and V expresses the model volume.

The generalized stacking fault energy  $\gamma_{gsf}$  calculations involved five planes, namely Basal, Prism I, Pyramidal I and II, and extension twinning planes. As shown in Fig. 1b, the model contains a 20-Å-thick vacuum gap and at least 12 Mg layers. The Mg atoms in the lower half layer were fixed in all directions but the upper half layer is free in the z-direction, and H which is located at the interface can relax in all directions. Further, the upper layer is displaced along serial vector  $\mathbf{u}$ , and the  $\gamma$ -line can be calculated from Eq. (7). Combining the unstable SF energy  $\gamma_{usf}$ , stable SF energy  $\gamma_{ssf}$  from  $\gamma$ -line, and materials elastic properties, the plastic properties of crystalline Mg can be explained (Andric and Curtin, 2018).

$$\gamma_{gsf} = \left(E_{\mathbf{u}} - E_{\mathbf{0}}\right) / A \tag{7}$$

where  $E_{\mathbf{u}}$  and  $E_{0}$  represent the DFT total energy with/without displacement along the vector  $\mathbf{u}$ , and A is the interface area.

#### 2.2.2. MD/MS simulations

Crack propagation and polycrystal 3D Mg models with/without H atoms were built based on Atomsk (Hirel, 2015). The cracking models considered two orientations, namely  $\{0001\}[10\overline{1}0]$  for cracking propagation analysis and  $\{10\overline{1}0\}[0001]$  for twining and dislocation emission. The size of  $\{0001\}[10\overline{1}0]$  cracking model is  $33 \times 29 \times 10$  nm, and a crack  $\sim 11.6$  nm is located on the left side of the model (Fig. 1c). Similarly, the  $\{10\overline{1}0\}[0001]$  cracking model has a 10.4 nm crack, its size is about  $31 \times 33 \times 9.6$  nm. The orientation of  $\{0001\}[10\overline{10}]$  cracking model is  $x-[10\overline{10}]$ ,  $y-[01\overline{10}]$ , and z-[0001], while that of  $\{10\overline{10}\}[0001]$  cracking model is x-[0001], y-[01 $\overline{1}$ 0], and z-[10 $\overline{1}$ 0]. The polycrystal Mg model contained 114,741 Mg atoms with 9 grains, sizing  $20 \times 5 \times 60$  nm. To satisfy the periodic boundary condition, the z-direction was fixed as  $[10\overline{1}0]$ , and the grains were randomly rotated around the z-axis (Fig. 1c). Based on the experimentally detected H concentration in Mg (Liu et al., 2017) and H-charging condition in this study, the H concentration in polycrystal Mg MD/MS model was determined as ~200 ppm which were randomly distributed at the TET sites in the grains (Supplementary Algorithm). For a concentration of 200 ppm in the MD/MS models, it could reflect the effect of H distributed inside the grain on the plastic deformation, while avoiding excessive H atoms diffusing to the grain boundaries (GBs). Two H atoms are placed before the crack tip of cracking MS models, besides, the  $\{10\overline{1}0\}[0001]$  cracking model was supplemented with six H atoms surrounding the crack tip to compare the effect of the H number on fracture. Owing to the grain size shortage (averaged 5.63 nm) of polycrystal Mg models, the temperature effect (300 K) promotes H atoms diffused towards the GBs. However, that is not the focus of this study. In addition, the interatomic potential used herein was that of the Mg-H embedded-atom method (EAM) (Smirnova et al., 2018). To guarantee the applicability of the EAM potential used, the  $\gamma_{gsf}$  was calculated by DFT and MD (Fig. A.1).

All models underwent conjugate gradient energy minimization to relax the structures, then the temperature ( $\sim$ 0 K) was initialized utilizing the velocity scaling method. The isothermal-isobaric ensembles were used to balance the pressure to 0 bars with a total relaxation time of 1000 ps. The most stable model was then employed to perform cracking or tensile simulation, the model applied 0.1 % deformation along the y-direction every 1 ps whose engineering strain rate was  $10^8 \, \rm s^{-1}$ . The x-direction of the model is set as shrink-wrapped non-periodic condition, the others are periodic condition. The corresponding stress (in MPa) was obtained from the average pressure along the deformation direction every 1 ps. The entire deformation of cracking and polycrystal Mg models are 10 % and 50 %, respectively.

To evaluate the fracture tolerance, the critical fracture toughness  $K_{Ic}$  (Eq. (8)), von Mises stress  $\sigma_v$  (Eq. (9)), and atomic shear strain  $\eta_s$  (Eq. (10)) were calculated.

$$K_{lc} = 1.122\sigma\sqrt{\pi a} \tag{8}$$

where  $\sigma$  is the uniaxial stress and a expresses the crack length.

$$\sigma_{v} = \sqrt{\frac{\left(\sigma_{xx} - \sigma_{yy}\right)^{2} + \left(\sigma_{yy} - \sigma_{zz}\right)^{2} + \left(\sigma_{zz} - \sigma_{xx}\right)^{2} + 6\left(\sigma_{xy}^{2} + \sigma_{yz}^{2} + \sigma_{xz}^{2}\right)}{2V^{2}}}$$
(9)

where  $\sigma_{ii}$  is the stress tensor and *V* indicates the atomic volume.

$$\eta_s = \sqrt{E_{xy}^2 + E_{xy}^2 + E_{xy}^2 + \frac{(E_{xx} - E_{yy})^2 + (E_{xx} - E_{zz})^2 + (E_{yy} - E_{zz})^2}{6}}$$
(10)

where  $E_{ij}$  is the Green-Lagrangian strain tensor.

#### 2.2.3. Polycrystal CPFEM

A 2D polycrystal CPFEM model containing 587 grains was generated according to the EBSD results (Groeber and Jackson, 2014), and a 3D CPFEM model with 5 elements thickness was built to compare the result difference between 2D and 3D CPFEM modeling, the models were shown in Fig. A.2. According to the results from Herrera-Solaz et al. (Herrera-Solaz et al., 2014), the number of grains exceeding 500 can reflect the macroscopic plastic deformation of Mg. The model was a gauge-length section of the tensile sample, whose size was  $500 \times 500 \, \mu m$ . The H-containing CPFEM model is parameterized with the combination of DFT stacking fault calculation and air FEM model fitting parameters. CPE4R elements (Fig. 1d) and periodic boundary condition were used in the FEM models (Xi et al., 2024), the size of each mesh was 1  $\mu m$  which was consistent with EBSD. The used crystal plasticity model (Kalidindi, 1998) was implemented as a UMAT in the ABAQUS. The multiplicative decomposition of the deformation gradient (F, Eq. (11)) and velocity gradient (L, Eq. (12)) were shown as follows.

$$\mathbf{F} = \mathbf{F}^{e} \mathbf{F}^{p} \tag{11}$$

$$\mathbf{L} = \dot{\mathbf{F}}\mathbf{F}^{-1} = \dot{\mathbf{F}}^{\ell}\mathbf{F}^{\ell} + \mathbf{F}^{\ell}\dot{\mathbf{F}}^{\ell}\mathbf{F}^{\ell} + \mathbf{F}^{\ell}\dot{\mathbf{F}}^{\ell}\mathbf{F}^{\ell} + \mathbf{F}^{\ell}\dot{\mathbf{F}}^{\ell}\mathbf{F}^{\ell}$$
(12)

where  $\mathbf{F}^e$  and  $\mathbf{F}^p$  represent the elastic (e) and plastic (p) part of the deformation gradient.

The plastic deformation was accommodated by slip and twining, it was composed of the slip in the parent phase (Lp sl, Eq. (13)), twin transformation (Lp tw, Eq. (14)), and the slip of the transformed region (Lp re-sl Eq. (15)).

$$\mathbf{L}_{sl}^{p} = \left(1 - \sum_{\alpha=1}^{N_{tw}} f^{\alpha}\right) \sum_{i=1}^{N_{sl}} \dot{\gamma}^{i} \mathbf{m}_{sl}^{i} \otimes \mathbf{s}_{sl}^{i} \tag{13}$$

$$\mathbf{L}_{\mathrm{bv}}^{p} = \sum_{\alpha=1}^{N_{\mathrm{bv}}} \dot{f}^{\alpha} \gamma_{\mathrm{bv}} \mathbf{m}_{\mathrm{bv}}^{\alpha} \otimes \mathbf{s}_{\mathrm{bv}}^{\alpha} \tag{14}$$

$$\mathbf{L}_{re-sl}^{p} = \sum_{\alpha=1}^{N_{\text{nw}}} f^{\alpha} \left( \sum_{i^*=1}^{N_{\text{sl}-\text{nw}}} \dot{\mathbf{j}}^{i^*} \mathbf{m}_{sl}^{i^*} \otimes \mathbf{s}_{sl}^{i^*} \right)$$

$$\tag{15}$$

where  $N_{sl}$   $N_{sl-tw}$ , and  $N_{tw}$  represent the number of potentially active slip systems in the untwinned crystal, the number of potentially active twin systems in the untwinned crystal, and the number of potentially active slip systems in each of the twinned regions of the crystal, respectively.  $f^{\alpha}$  is the volume fraction of the twin system  $\alpha$ ,  $f^{\alpha}$  is the rate of the volume fraction transformation.  $\gamma_{tw}$  is the characteristic shear of the twining mode (0.129).  $\bf s$  and  $\bf m$  stand for the unit vectors in the slip and normal direction to the slip plane, respectively.

The plastic slip rate  $(\dot{\gamma}, \text{Eq. } (16))$  for the given slip system follows a power-law (Zhang et al., 2023), similarly the twinning rate  $(\dot{f}, \text{Eq. } (17))$  follows a vicious law. When the volume fraction of the twin exceeds 0.8 (Fernández et al., 2011), the twin transformation will be stopped (Eq. (18))

$$\dot{\gamma}^i = \dot{\gamma}_0 \left(\frac{|\tau^i|}{g^i}\right)^{\frac{1}{m}} \operatorname{sign}(\tau^i) \tag{16}$$

$$\dot{f}^{a} = \dot{f}_{0} \left( \frac{\langle \tau^{a} \rangle}{g^{a}} \right)^{\frac{1}{m}} \text{with } \langle \tau \rangle = \begin{cases} \tau & \text{if } \tau \geq 0 \\ 0 & \text{if } \tau < 0 \end{cases}$$
 (17)

$$\dot{f}^{\alpha} = 0 \text{ if } \sum_{\alpha=1}^{N_{\text{hw}}} f^{\alpha} \ge 0.80$$
 (18)

where  $\dot{\gamma}_0$  is a reference shear strain rate, g expresses the critical resolved shear stresses,  $\tau$  is the resolved shear stress of systems, m is the rate-sensitivity exponent, and i and  $\alpha$  denote the slip and twin systems, respectively.

Green-Lagrange strain tensor  $\mathbf{E}^e$  and the symmetric second Piola-Kirchhoff stress tensor  $\mathbf{S}$  can be calculated from Eqs. (19)–(23).

$$\mathbf{E}^{e} = \frac{1}{2} \left( \mathbf{F}^{e^{T}} \mathbf{F}^{e} - \mathbf{I} \right) \tag{19}$$

$$\mathbf{S} = \left(1 - \sum_{\alpha=1}^{N_{\text{bw}}} f^{\alpha}\right) \mathbf{S}^{\text{parent}} + \sum_{\alpha=1}^{N_{\text{bw}}} f^{\alpha} \mathbf{S}^{\alpha}$$
(20)

$$S^{\text{parent}} = \mathbb{C}E^e$$
 (21)

$$\mathbf{S}^a = \mathbb{C}^a \mathbf{E}^e$$
 (22)

$$\mathbb{C}_{ikl}^a = \mathbb{C}_{pars}^a Q_{ip}^a Q_{iq}^a Q_{kr}^a Q_{is}^a \tag{23}$$

where **I** is the second-order identity tensor, C and  $\mathbb{C}^{a}$  indicate the fourth-order elastic stiffness tensor of the crystal in its original orientation or after twining.

The evolution of the critical resolved shear stress  $g^i$ ,  $g^a$ , and  $g^{i*}$  for both slip, twin, and re-slip systems are given by Eqs. (24)–(26).

$$\dot{g}^{i} = q_{sl-sl} \sum_{i=1}^{N_{sl}} h_{0j} \left( 1 - \frac{\tau^{j}}{\tau_{sat}^{j}} \right)^{a_{sl}} \left| \dot{\gamma}^{j} \right| + q_{tw-sl} \sum_{\beta=1}^{N_{nv}} h_{0tw} \left( 1 - \frac{\tau^{\beta}}{\tau_{sat}^{tw}} \right)^{a_{tw}} \left| \dot{\gamma}^{\beta} \right| \tag{24}$$

$$\dot{g}^{\alpha} = q_{tw-tw} \sum_{\beta=1}^{N_{tw}} h_{0tw} \left( 1 - \frac{\tau^{\beta}}{\tau_{sat}^{tw}} \dot{f}^{\alpha} \gamma_{tw} \right) \tag{25}$$

$$\dot{g}^{j^*} = q_{sl-tw} \sum_{j=1}^{N_{re-sl}} h_{0j} \left( 1 - \frac{\tau^j}{\tau_{sat}^j} \right)^{a_{sl}} \left| \dot{\gamma}^j \right|$$
(26)

where coefficient q indicates the latent-hardening contribution to slip/twin between systems, the  $q_{tw-sl}$  is the contribution induced by twining, in this study, the contribution of slip to twin  $q_{sl-tw}$  is assumed to be 0,  $q_{sl-sl}$  and  $q_{tw-sl}$  is 1.0 and 3.0 respectively (Sedighiani et al., 2020).  $\tau_{sat}$  is the saturation stress, and  $h_0$  is the initial hardening rate, j represents the different system.

#### 3. Result

#### 3.1. Effect of H on the mechanical behavior of Mg

To elucidate the effect of H ion types and contents on the plasticity of Mg, SSRTs were performed in H-containing environments for quantitative research. The stress-strain curves were shown in Fig. 2. In contrast to the traditional HE and H-induced cracking of steel, the ductility of Mg increased in atomic H environments. Specifically, The UTS of Mg in air was  $117.94\pm1.07$  MPa and the elongation was  $19.46\pm0.98$  % (in Fig. 2a). Whereas the elongation of the Mg in the atomic H environment improved, reaching  $22.06\pm0.31$  %. Stampella et al. (1984) also performed the catholically polarized SSRT and found there is no embrittlement and cracking, they attributed it to the covered Mg(OH)<sub>2</sub> film which can completely disrupt the H diffusion into the matrix. However, it is reported that the film on the Mg surface (anodic polarization which adequately provides  $Mg^{2+}$ ) was MgO and Mg(OH)<sub>2</sub> porous mixture (Song and Unocic, 2015). The produced H may induce the film to be more porous and cracked, and then diffuse into the Mg substrate through metallurgical defects. When there was a high cathodic potential ( $-1.6 \, V_{SCE}$  in this study) which could accelerate H permeation, the H was detected in the presence of the oxide film (Ajito et al., 2023). Theoretically, catholic polarization only referred to the H reduction and did not involve the Mg cationization (Mg<sup>2+</sup>). In an alkaline environment, the species Mg\*OH is another form of Mg<sup>+</sup> (Huang et al., 2020), even if Mg(OH)<sub>2</sub> was generated on the surface it would accelerate the reduction of H (2 or 3 times faster than that of Mg surface) (Salleh et al., 2015). Meanwhile, assuming there is no H entering the Mg matrix, the SSRT result should be similar to that in the air. Therefore, the elongation enhancement was attributed to the permeated H atoms.

Although the strain hardening rate (plastic region) of the Mg in the atomic H environment was similar to that in air (Fig. 2b), its volatility increased significantly. In the case of rapid strain, the multiple high peaks in the strain-hardening rate curve indicated twins occurred in the plastic stage (Sahoo et al., 2020; Sedaghat and Abdolvand, 2021). Therefore, the atomic H-charged sample in the plastic stage implies that some twins appeared during the mechanical deformation, which could coordinate the deformation. To verify

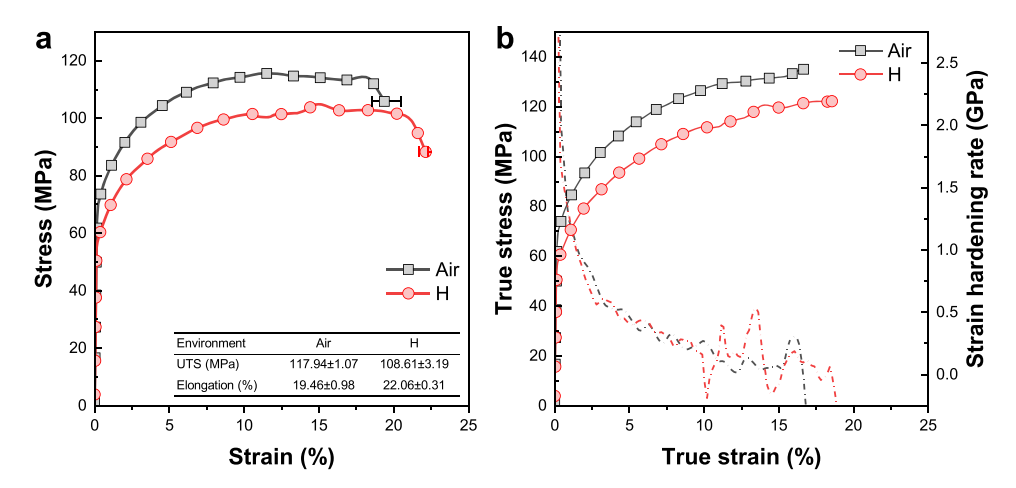


Fig. 2. SSRT of Mg in different environments: (a) engineering stress-strain curve; (b) true stress-strain curve and strain hardening rate.

the twinning of Mg in different environments, the EBSD tests were performed (Fig. 3). Except for pure Mg, the AZ31 Mg alloys were also tested and characterized (Fig. A.3-A.4). It could be found that the ductility enhancement of AZ31 Mg alloys with large-grain (>3 mm) was more obvious (improved by  $\sim$ 5.8 % than stretched in air). When pure Mg was used to compare the H effect on ductility, the average grain size of pure Mg significantly decreased to 22.44  $\mu$ m (Max Feret Diameter, Fig. 3a and d), its enhancement in elongation is only 2.60 %. Meanwhile, the length of GBs significantly increased which is favorable for H distribution. As shown in Fig. 3f, the orientation of pure Mg along the z-direction is {0001}, and its exposure surficial orientation is mainly{10 $\overline{10}$ }.

Comparing the microstructure of Mg in air or atomic H environment, it could be seen from Fig. 3b, c, and e that there were both twining happened. Whereas, the twining region in the air was mainly focused on the bottom-right corner, its area fraction of twins is near 1.06 %. When the Mg samples were stretched in the atomic H environment, the number of grains undergoing twining increased significantly. Different from the Mg deformed in air whose twins mainly occurred in  $\{02\overline{23}\}$ , while the twins of Mg stretched in atomic H environment were widely found in  $\{\overline{2750}\}$ ,  $\{14\overline{50}\}$ , and  $\{11\overline{20}\}$ . Especially for the  $\{\overline{2750}\}$  grain (Fig. 3e), the plane of twins was  $\{0001\}$ . Besides, the twin area fraction of Mg in the atomic H environment was greatly improved by 167 %, which promoted plastic deformation.

#### 3.2. H adsorption and diffusion on Mg surface and in the GBs

The adsorption and diffusion of H on Mg were studied to distinguish the susceptibility of orientations ( $\{0001\}$ ,  $\{10\overline{1}1\}$ , and  $\{10\overline{1}0\}$ ). A total of 21 surficial sites (FCC, HCP, top, bridge, and hollow) and interstitial sites (octahedral interstice O-site, and tetrahedral interstice T-site) were included (Fig. 4). The surface energy was calculated to corroborate the accuracy of models. It could be found that the surface energy of the most easily formed surface  $\{0001\}$  (0.528 J  $m^{-2}$ ) was lower than those of  $\{10\overline{1}1\}$  (0.640 J  $m^{-2}$ ) and  $\{10\overline{1}0\}$  (0.656 J  $m^{-2}$ ) (Tran et al., 2016).

Thermodynamically, not all adsorption sites were spontaneous, for instance, the top site on all orientations was endothermic, with values of 0.48 eV  $H^{-1}$  on {0001} and 0.21 eV  $H^{-1}$  on {10 $\overline{10}$ }. For the {0001}, Sprunger and Plummer (1991) experimentally prepared a single-crystal Mg with this orientation, and emitted a single H atom to its surface. The H adsorption energy was determined to be -0.27 eV by the Raman peak which was consistent with the DFT calculations in this study (-0.29 eV  $H^{-1}$ ) (Baldi et al., 2009). Among the three orientations (Fig. 4), the adsorption energy of the { $10\overline{11}$ }<sub>FCC</sub> site was the lowest, reaching -0.40 eV  $H^{-1}$ . More sites could stably adsorb H atoms on the { $10\overline{10}$ }, and their average adsorption energy was -0.31 eV  $H^{-1}$ . Both the FCC and HCP sites were stable

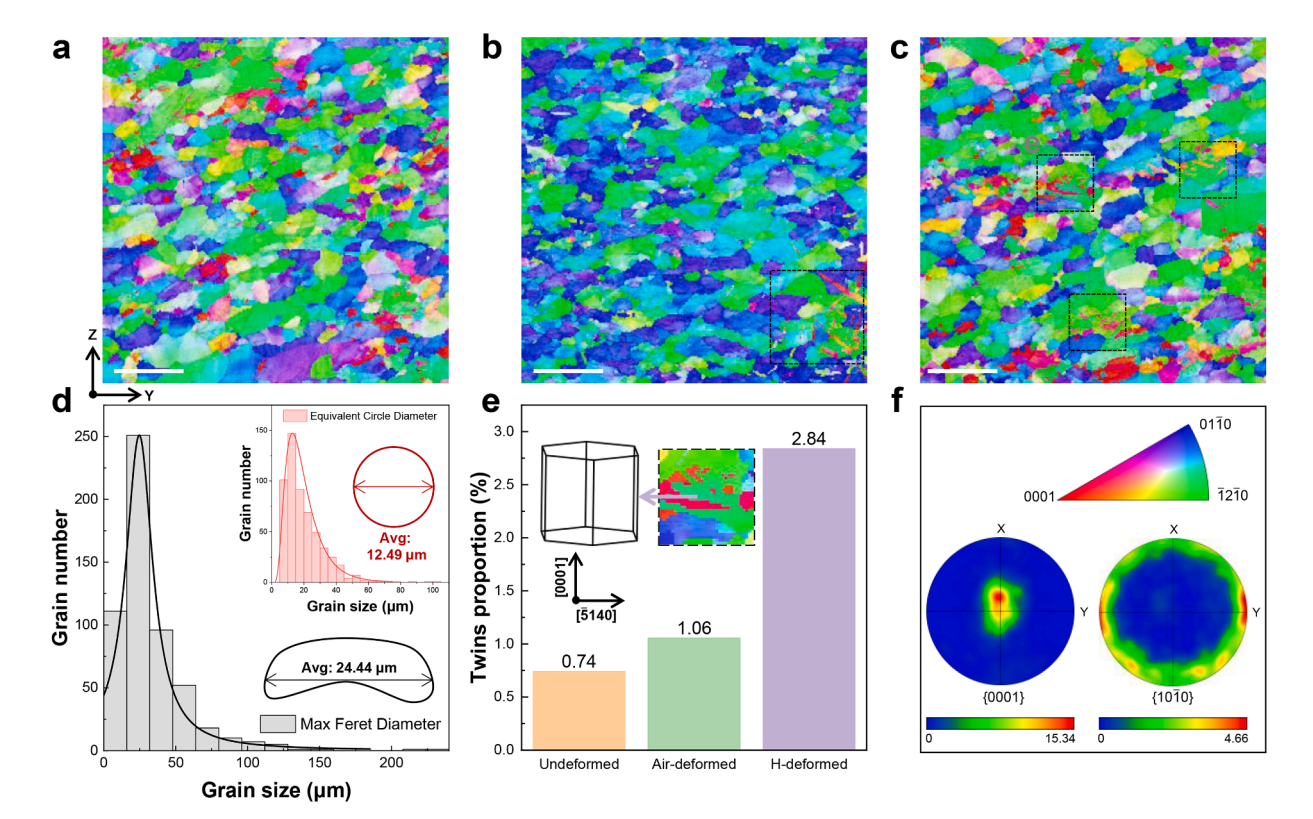


Fig. 3. The microstructure of Mg strained in different environments: (a) Undeformed; (b) Air; (c) Atomic H; (d) The grain size distribution; (e) Twins area proportion compared with total region; (d) Orientation legend and texture pole analysis; All the length bar is  $100 \mu m$ , and coordinate system is the same as that of SSRT sample in Fig. 1.

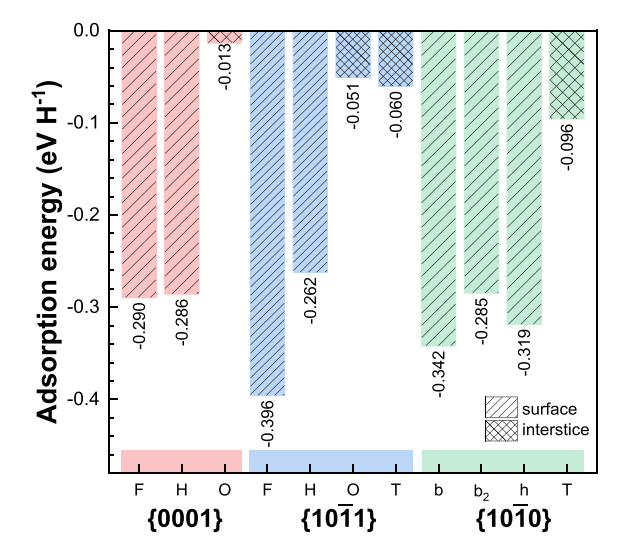


Fig. 4. H adsorption energies of spontaneous sites on different Mg surfaces: F denotes FCC, H is HCP, O represents O-site, T stands for T-site, b indicates bridge, and h expresses hollow.

on  $\{0001\}$  and  $\{10\overline{1}1\}$ ; however, the bridge sites were more stable on  $\{10\overline{1}0\}$ . The specific location of all stable sites, irrespective of the exothermic or endothermic reactions, were shown in **Fig. A.5**. Comparing the dissolution energies of the interstice, it could be seen that only  $\{10\overline{1}1\}$  had two stable interstitial sites. The interstitial sites inside the subsurface were weaker than those on the surface. The position with the highest dissolution energy among the interstitial sites was the T-site inside the  $\{10\overline{1}0\}$ , which was 0.05–0.09 eV higher than that inside the remaining two orientations. During the structural optimization, some initial sites on surfaces migrated to stable positions, these positions were listed in Table A.2.

Not all thermodynamic stable sites can absorb H atoms simultaneously. As  $H_2$  was formed owing to their strong binding energy, the relationship between the site-to-site distance and H potential energy (Fig. 5) resulted in only certain sites being able to adsorb H simultaneously. The maximum H adsorb ability of orientations was determined. For the three sites (top, FCC, and HCP) on {0001}, the safe distance of the adsorption site with -0.29 eV  $H^{-1}$  was 2.18 Å. Hence, the H atoms at the {0001} $_{FCC}$  and {0001} $_{HCP}$  sites would generate  $H_2$  and could not penetrate the matrix. Similarly, both the adsorption sites on {10 $\overline{1}$ 1} were exothermic, but there was not a sufficient distance (1.844 Å) between them to avoid forming the  $H_2$ . For co-adsorption, the adsorption energies of the sites must be greater than 0.5 eV  $H^{-1}$ . Therefore, the number of effective adsorption sites of {10 $\overline{1}$ 1} was only 5 nm $^{-2}$ , which was the lowest among all orientations. What's more, the adsorption energy of {10 $\overline{1}$ 0} $_{top}$  site was positive and the distance between them was 1.76 Å; so, it was easy to combine H atoms with the  $b_2$  site. Since the distance between the  $b_2$  and hollow site was even shorter, i.e., only 1.24 Å, the

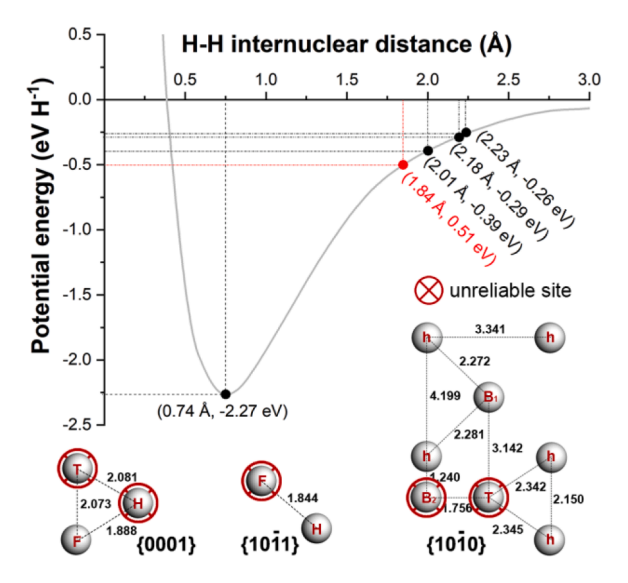


Fig. 5. Effective H adsorption sites on Mg surfaces.

adsorbed H also could form  $H_2$ . To adsorb more H atoms simultaneously, the optimal adsorption scheme was to avoid adsorbing H at the  $b_2$  site. Based on this scheme, the maximum theoretical number of H adsorbed on  $\{10\overline{1}0\}$  reached  $18 \text{ nm}^{-2}$  which was higher than that on  $\{0001\}$  ( $11 \text{ nm}^{-2}$ ).

As another important diffusion admittance for H atoms, GBs were also considered (Ji et al., 2021). The results (in Table 1) showed that the interstitial sites at the severely distorted region of the GBs could seize H atoms; however, most of the interstices were weaker than the subsurface of the surface. In particular, the dissolution energy of a site inside  $\{10\overline{1}0\}//\{0001\}$  reached up to a magnitude of 1.061 eV  $H^{-1}$ , which was favorable for the aggregation of H atoms.

To determine whether H diffused easily into the Mg matrix, TSS was utilized to investigate the energy barrier. Fig. 6 showed the energy barrier of an H atom diffusing from the surface to the interior. According to the energy barrier,  $\{10\overline{1}0\}$  was extremely vulnerable to H atoms and its diffusion energy barrier was only 0.156 eV  $H^{-1}$ . The entire diffusion in  $\{10\overline{1}0\}$  was straightforward. Considering the similar internal symmetries, H atoms diffused easily into the deep interior. Although the number of effective H adsorption sites on  $\{0001\}$  was close to that on  $\{10\overline{1}0\}$ , it had the highest diffusion barrier (Gerashi et al., 2022). Moreover, the diffusion of H on  $\{10\overline{1}1\}$  was similar to that on  $\{0001\}$  (0.421 eV  $H^{-1}$ ). Therefore, considering that fewer H atoms were absorbed on its surface, the  $\{10\overline{1}1\}$  was deemed to be the orientation with the strongest resistance to H.

Since there was an extremely stable site of dissolution inside the GBs, the TSS of H atoms diffusing from the surface to interstice at the interface was also studied (Fig. 7). While diffusing into the interior by means of GBs, the H atoms must overcome two energy barriers:  $0.272 \text{ eV } H^{-1}$  at a distance of 2.96 Å from the surface; and  $0.379 \text{ eV } H^{-1}$  inside the GB interior. After overcoming the first barrier, the H atom reached an energy minimum. Fig. 7b and c summarized the path taken by an H atom placed on the surface while diffusing inward. During its diffusion, the H atom passes through the T-site with an energy of 0.12 eV. Then, the atom required further diffusion to pass through the bridge site, whose energy barrier was 0.272 eV. After that, the H atom spontaneously moved to the most stable site with the largest voids. However, if the H atom continuously diffuses inward, it must overcome the energy barrier of 0.379 eV. Due to the lower energy barrier on the other side, the H atom could not penetrate the interior but escaped to the surface instead. Unless the H concentration was high, the H atom would be forced to diffuse inward depending on the chemical potential of the H atoms (in the solution). Clearly, easier than the  $\{0001\}$  and  $\{10\overline{1}1\}$  orientations, the GBs were still the second choice for H diffusion.

#### 3.3. DFT calculation interpretation for Mg with H

To explain the mechanism of H-induced ductility that occurred when Mg was stretched in H environments, the elastic stiffness (Eq. (6), Fig. A.6-A.8) and the  $\gamma_{gsf}$  of Mg with/without H atoms were calculated. From Table A.3, it could be seen that the normal component ( $c_{11}$ - $c_{66}$ ) of twin-{0001} without H stiffness tensor had increased by 0.5–19.4 GPa than pure {0001} without H, while their shear component ( $c_{12}$  and  $c_{13}$ ) descends drastically. When H atoms were distributed at the twin-{0001} interface, their elastic constant was partially recovered. Owing to the anisotropy, the mechanical properties of crystals in each direction were too different to be directly compared. Therefore, the Hill model (Hill, 1952) was used to synthesize the elastic constants in all directions, which could determine the effect of additional H ingress on the moduli (Fig. 8a). Besides, the Hill model balanced Voigt and Reuss approximate methods, their results were shown in Fig. A.9 and Table A.4.

The bulk modulus considered the volume reduction and combined the effects in various directions. When H atoms entered the  $\{0001\}$ , its bulk modulus decreased by only  $\sim$ 0.2 GPa than  $\{0001\}$  without H (Fig. 8). Although exhibiting the lowest corrosion sensitivity and maximal bulk modulus (42.2 GPa), the bulk modulus of  $\{10\overline{1}1\}$  with H atoms had a  $\sim$ 13.5 % deterioration compared to Mg- $\{10\overline{1}1\}$  without H, reaching 36.2–37.0 GPa. The bulk modulus of  $\{10\overline{1}0\}$  with a single H atom decreased slightly than pure  $\{10\overline{1}0\}$ , whereas it reached 36.8 GPa when 2H atoms entered. This improvement did not exceed that of the original crystal, which was still 0.4 GPa lower. The bulk modulus of the twin- $\{0001\}$  without H (only 34.2 GPa) demonstrated that although twinning promoted deformation, it was enormously reduced by 8.3 % than  $\{0001\}$ . Inversely, the H introduction did not induce a decrease in the bulk modulus; instead, it restored its bulk modulus to that of  $\{0001\}$ , close to 37.1 GPa (red region in Fig. 8a). The bulk modulus of the model with  $H_{O}$  site increased by 1.2 GPa but did not recover to that of  $\{0001\}$ .

It can be seen from Fig. 8b that the energy of twin-{0001} rose by 1.09 eV when H was set into the O-site (without deformation). When the strain matrix  $\varepsilon = (0, 0, 0, 0.01, 0.01, 0.01, 0.01, 0.01)$  was applied to the model (Fig. 8b, red arrow), the energy of twin-{0001} dropped to the position where H was at the T-site. In practice, regardless of the strain value, it was adequate to expand the unit cell size in both  $\varepsilon_{xz}$  and  $\varepsilon_{yz}$  directions simultaneously. These expansions indicated atomic slips might occur on the Pyramidal II plane. However, all mechanical moduli calculations were based on the micro-strain; therefore, these results still belonged to the elastic region parameters.

For the plastic stage, the  $\gamma_{gsf}$  can better represent the effect of H on the deformation (Fig. 9). Except Prism I plane, the  $\gamma_{gsf}$  of the other four slip planes were decreased. The  $\gamma_{usf}$  determined the activation barrier for dislocation nucleation which affected the plastic deformation. Comparing the  $\gamma_{usf}$  of all slip planes, it could be found that Basal-{0001} exhibited the lowest  $\gamma_{usf}$  which was only 88.7 mJ

**Table 1**Dissolution energy of H atom in Mg GBs.

GBs	different sites (eV $H^-$	1)		
{1010}//{0001}	-0.043	-0.058	-1.061	-0.051
$\{10\overline{1}0\}//\{10\overline{1}0\}$	-0.186	-0.057	-0.182	-0.069

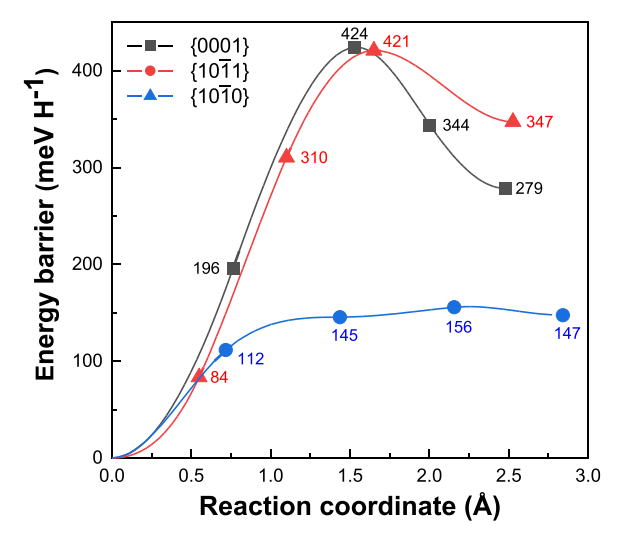


Fig. 6. TSS for H diffusion on Mg surfaces.

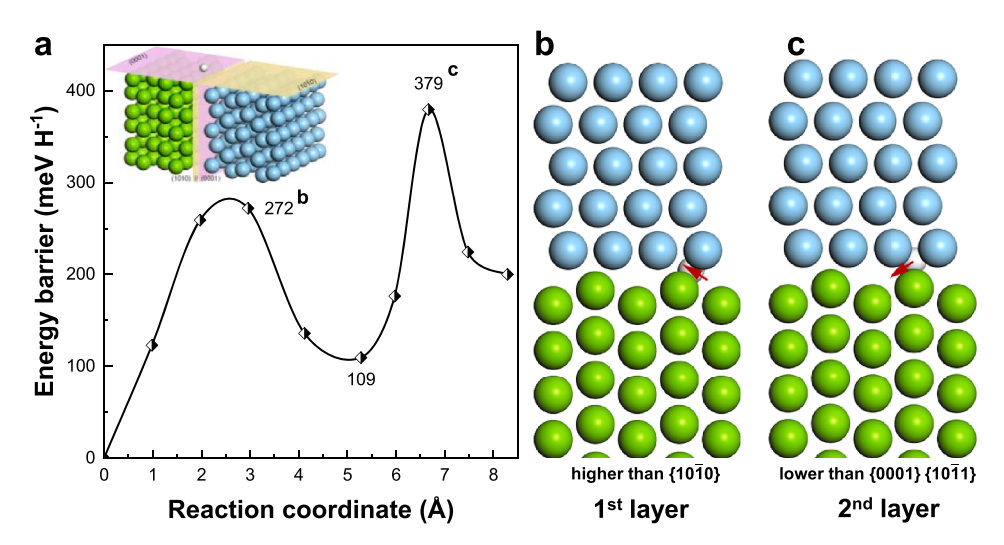


Fig. 7. Energy barrier and diffusion path of H atom through GBs.

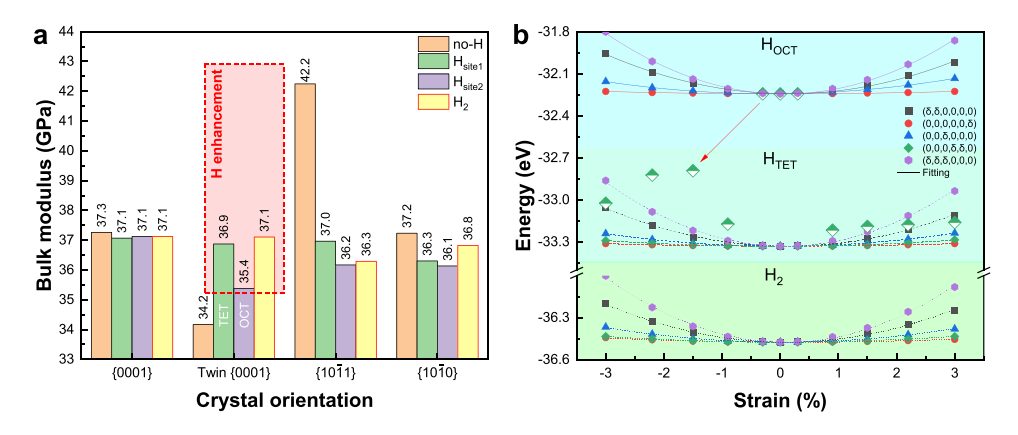


Fig. 8. Bulk modulus of crystals with different orientations and energy fluctuation of twin- $\{0001\}$  with H atoms under micro-strain.  $\varepsilon$  is the applied strain matrix where  $\delta$  is the specific strain value.

 $m^{-2}$  along [10 $\overline{10}$ ] (Yin et al., 2017). After bypassing this barrier, the  $\gamma_{ssf}$  of {0001} reached 25.2 mJ  $m^{-2}$ , resulting in the stacking fault. However, when the H entered the slip interface of {0001}, their  $\gamma_{usf}$  (72.3 mJ  $m^{-2}$ ) decreased by 18.5 % compared to {0001} without H. This indicated that the {0001} with H was more easily forming stacking faults. Meanwhile, the  $\gamma_{ssf}$  of {0001} became -7.13 mJ  $m^{-2}$ , this negative value demonstrated the formed stacking faults were more stable than the initial HCP structure. Furthermore, the  $\Delta \psi$  ( $\gamma_{usf}$  -  $\gamma_{ssf}$ ) represented the energy required for structure reversal, it is found that the H-induced {0001} stacking fault was 79.4 mJ  $m^{-2}$  which was 25 % higher than that of the {0001} (63.5 mJ  $m^{-2}$ ).

In terms of the other H-promoted slip planes, the  $\gamma_{usf}$  of Pyramidal II, extension twining, and Pyramidal I plane with H were 239.1 mJ  $m^{-2}$ , 314.0 mJ  $m^{-2}$ , and 436.5 mJ  $m^{-2}$  respectively. Compared with the planes without H, the average  $\gamma_{usf}$  reduction ratio of planes with H was ~3.05 %. Although the slip direction [10 $\overline{1}$ 0] on the extension twinning plane (Fig. 9e) exhibits the lowest  $\gamma_{gsf}$  (318 mJ  $m^{-2}$ ), there is no stable stacking fault point. This indicates the {10 $\overline{1}$ 2} plane can easily slip, while the stacking fault direction is [ $\overline{5}$ 413]. Despite the SF generated, the  $\Delta\psi$  of Pyramidal I and II planes was low, which were only 29.1 mJ  $m^{-2}$  and 2.85 mJ  $m^{-2}$ . As for the Prism I slip plane, the intrusion of the H atom improved the energy barrier of the minimum slip path [ $2\overline{1}\overline{1}$ 0]/3 from 258.7 mJ  $m^{-2}$  to 270.4 mJ  $m^{-2}$  (4.5 %). There also existed SF on the Prism I plane along the [ $2\overline{1}\overline{1}$ 3], whereas its required  $\gamma_{usf}$  was as high as 504.9 mJ  $m^{-2}$ . In addition, the  $\gamma_{ssf}$  of this SF was only 8.3 mJ  $m^{-2}$ , which meant it was extremely stable once it was formed. Comprehensively, as far as Mg slip was concerned, it was most likely to occur on the Basal plane, followed by Pyramidal II and Prism I plane (extremely close).

#### 3.4. Cracking propagation simulation with H atoms

Apart from twining, the crack propagation also profoundly affected the elongation of Mg. Therefore, the  $\{0001\}[10\overline{1}0]$  and  $\{10\overline{1}0\}$  [0001] cracking models with/without H atoms were compared to clarify the influence of H on cracking (Fig. 10). Comparing their true stress-strain curve shown in Fig. 10a, it could be found that the required stress of the  $\{0001\}$  for slipping was significantly lower than that of the  $\{10\overline{1}0\}$ .

When the applied stress reached 1.04 GPa, the stress concentrated on the crack tip promoted the cleavage cracking on {0001} along [ $10\overline{1}0$ ], the strength decreased significantly after 4.49 % strain (Fig. 10a black and b). However, the cracking mode was changed after H permeated. It could be found from Fig. 10c that there was an obvious cracking tip deflection. The high positive  $\sigma_{xy}$  region (in red) of the H-{0001} crack tip was larger than that of {0001} without H. Combined with the position of H atoms, It can be speculated that the distribution of H not only changed the direction of crack propagation (in zig-zag), but also enhanced the stress in their adjacent region.

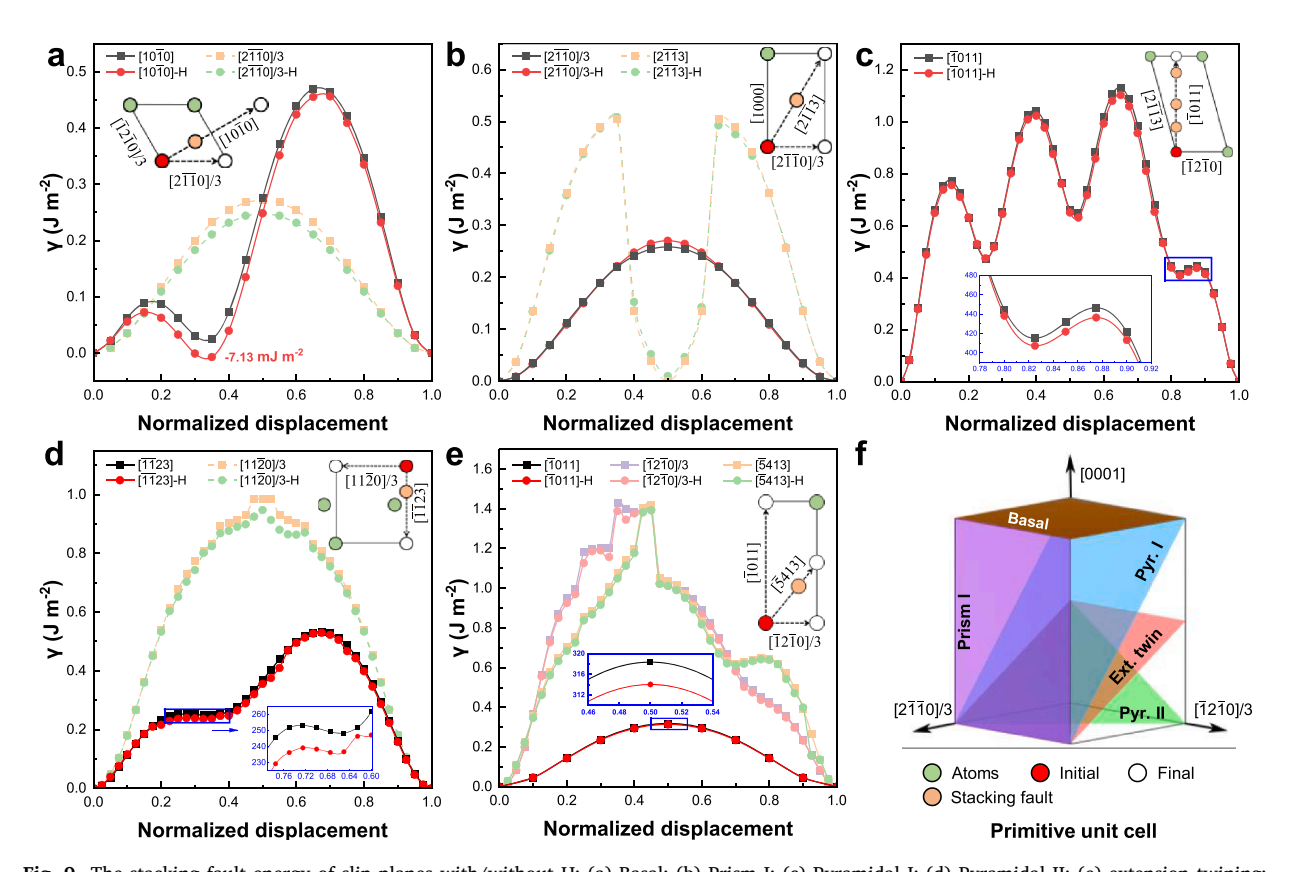
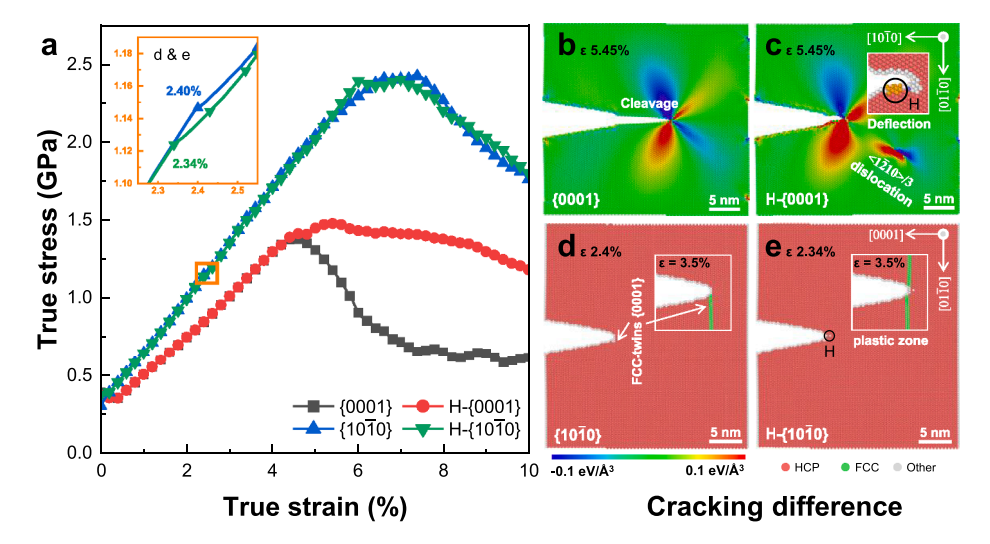


Fig. 9. The stacking fault energy of slip planes with/without H: (a) Basal; (b) Prism I; (c) Pyramidal I; (d) Pyramidal II; (e) extension twining; (f) schematic.



**Fig. 10.** Crack propagation of models with/without H atoms: (a) true stress-strain curve; cracking morphologies: (b-c) shear stress  $\sigma_{xy}$  on the {0001} [ $10\overline{10}$ ] and (d-e) twining of { $10\overline{10}$ }[0001].

This enhancement did not cause the degradation of  $\{0001\}$ , but reversely emitted the dislocation in  $[10\overline{1}0]$ , further promoting its coordinated deformation.

For  $\{10\overline{1}0\}$  plane, its cracking resistance was stronger than that of  $\{0001\}$  (Fig. 10a blue and green). Except for the plastic zone found at the crack tip, the addition of H atoms did not change the cracking mode of  $\{10\overline{1}0\}$ . During the deformation, there was obvious SF between  $\{0001\}$  planes which own the lowest  $\gamma_{usf}$ . Differently, the 2H distributed along the cracking path promoted the early emission of SF ( $\sim$ 0.06 %, Fig. 10e). Under the same strain (3.5 %), the SF number of H- $\{10\overline{1}0\}$  was slightly greater than  $\{10\overline{1}0\}$ . With the stretch enhanced,  $\{10\overline{1}0\}$  did not cleave but emitted another direction SF (Fig. 11c).

To distinguish whether the H position and concentration affected the Mg SF emission, a model with 6H surrounding the crack tip was simulated. Unexpectedly, the surrounding 6H atoms did not promote the early occurrence of SF, but rather delayed it. At a strain of 2.54 %, the  $\{10\overline{1}0\}$ -6H emitted the first SF on the  $\{0001\}$  plane. Although the SF was delayed, it can be seen from Fig. 11f that more H atoms contributed to the large stable presence of  $\{0001\}$ -SF.

In addition, Fig. 11g intuitively showed the situation of models (0H, 2H, and 6H) when the first SF was emitted (cracking). Compared with the 0H model (2.41 %), the 2H along the cracking underwent SF earlier (2.34 %), which could be inferred that a small amount of H is beneficial to the slip of dislocation (HELP). The surrounding 6H was delayed by  $\sim$ 0.20 %, however, there was no difference in the atom number of SF. Therefore, the von Mises stress (Eq. (9)) was utilized to compare the SF trigger stress condition. It could be found from Fig. 11h that the addition of H atoms near the crack tip definitely improved the critical von Mises stress of cracking propagation, especially for the 6H model (4.23 GPa, improved by 5.94 % compared to 0H model). Emitting the SF greatly reduced the von Mises stress, but the atoms with 6H were still slightly higher than the atoms without H. Under the same strain condition, the H-affected crack tips need more stress applied, so the critical fracture toughness  $K_{Ic}$  (Eq. (8)) was calculated (Table 2). Specifically, the  $K_{Ic}$ 

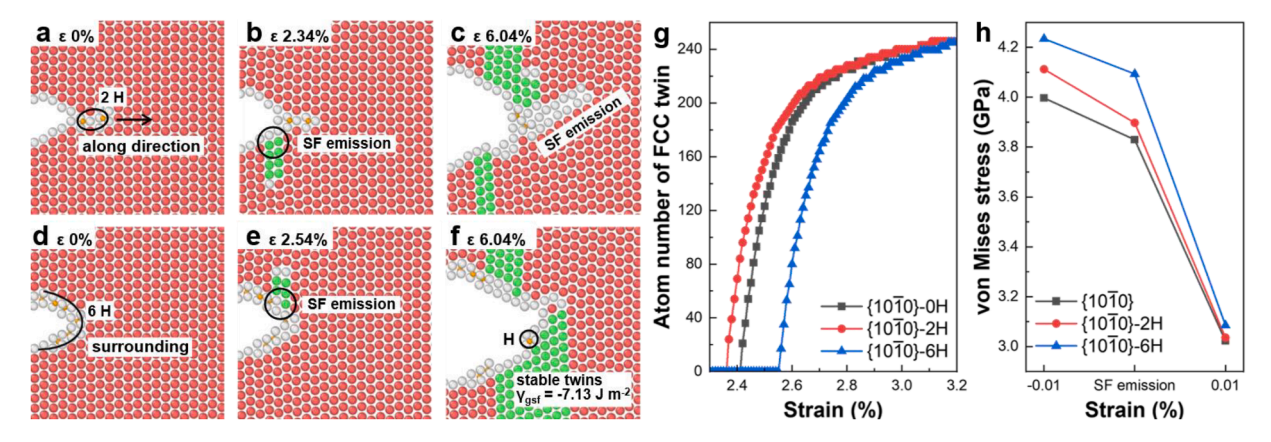


Fig. 11. The SF emission of  $\{10\overline{10}\}[0001]$  with different H atoms: (a-c) 2H distributed along the cracking direction; (d-f) 6H surrounding the crack tip; (g) Atom number of twin with strain applied; (h) The critical von Mises stress change within 0.01 % strain before/after SF emission.

of  $\{0001\}[10\overline{1}0]$  did not change, its cracking resistance was attributed to the deflection of the propagation path. The  $K_{Ic}$  of  $\{10\overline{1}0\}$  [0001] was higher than that of  $\{0001\}[10\overline{1}0]$ , and it was obviously changed after the H addition. In terms of 2H, the  $K_{Ic}$  dropped to 0.2229 MPa  $\sqrt{m}$ , while the 6H inversely increased to 0.246 MPa  $\sqrt{m}$  (6.4 % improvement compared to 0H model).

#### 3.5. Polycrystal Mg deformation with H atoms inside grains

To study the coordinated deformation differences, polycrystal Mg models with/without H were constructed, their stress-strain curve, SF number, and slip morphologies were summarized in Fig. 12. Constrained by the grain size of the MD/MS models, the temperatures were set as 0 K to keep the H distributed inside the grains. Combined with Fig. 12a (stress magnification frame), b (blue frame), and c, it could be confirmed that the polycrystal Mg-H model emitted SF earlier (at a strain of 2.23 %) than Mg model. Notably, the occurrence of SF was associated with a reduction in the strength of the model to some extent (such as Mg-H model at strains of 2.2 %), the most obvious strength decrease was the polycrystal Mg after the strain reached 4.92 %. The atom number of SF was increased, while their strength dropped by ~40 MPa, reaching 1.53 GPa. This strength platform of polycrystal Mg maintained around 1 % strain (Fig. 12a green frame).

As the strain was applied, both models reached their UTS at a strain of ~7.23 %. However, ~200 ppm H did not affect the strength of the Mg-H model, which only improved from 1.884 GPa to 1.886 GPa. Afterward, the strength of Mg without H dropped rapidly until voids were generated at a strain of 11.37 %. Conversely, even with 50 % strain, the polycrystal Mg-H model still did not show voids (Fig. 12f), its strength drop was also lower than that of the Mg without H. The atomic strain was summarized in Fig. 12d and e. Although the SF number of models was increased, the manner of SF emission was markedly different. Specifically, the SF growth source of polycrystal Mg was the initial {0001} along the strain direction. However, the H-containing Mg was mainly the occurrence of symmetric twins, not only the SFs. As shown in Fig. 12e, the twin on the left (red region) contained massive small twins (not SF), and these small twins were also growing (Fig. A.10). Therefore, the high strain of the Mg-H model was mainly attributed to the formation of symmetric twins, rather than simply SFs (Fig. A.11).

Considering the periodic boundary of MD/MS models, their grain size was limited and the added H atoms were easily diffused into GBs at 300 K which weakened the ductility enhancement. Thereby, the plastic deformation of polycrystal Mg models with EBSD-detected grain information was studied by CPFEM, and their results were summarized in Fig. 13. It could be found that the twining volume fraction of Mg in the atomic H environment is greater than that of Mg in the air. The highest twining volume fraction of Mg with H is 0.65, while that in air was 0.57. Although the 2D CPFEM model simplified the stress, there was no significant difference in equivalent plastic strain and von Mises stress morphology compared with the 3D models (Fig. A.12).

Based on the DFT and MD results, the H-{0001} demonstrated an important contribution to plastic deformation, so the relative activity of {0001} was summarized in Fig. 13b. It could be seen that the relative activities of most grains of Mg deformed in the air were distributed among 0.0–0.2, while under same microstructure condition, that of Mg stretched in atomic H was near 0.4. However, this obvious difference mainly happened with strain lower than 2 %. Besides, all parameters of Mg deformation in the air model in Eqs. (11)–(26) were calibrated from experimental stress-strain curve (Fig. 13c black). Differently, that of Mg deformed in atomic H environment combined the DFT  $\gamma_{gsf}$  and parameters in air (the scaling is consistent with  $\gamma_{gsf}$  before/after H permeation, **Supplementary CPFEM**). According to the highly coincident experimental and simulated stress-strain curves (Fig. 13c), the correctness of the atomic mechanism deducted by MD/MS simulation was confirmed. Meanwhile, under the same deformation, the highest von Mises stress of Mg in the air (137.2 MPa) is higher than that of Mg in atomic H (126.0 MPa).

The relative activities of important slip planes were shown in Fig. 14a. It could be found that the main slip planes were the Basic and Prism I planes. When the system was deformed in air, the preferred slip system was Prism I, its relative activity decreased with strain applied. Meanwhile, the relative activity of Basal- $\{0001\}$  was slowly increased and finally maintained at  $\sim 0.227$ .

However, the slip mode of Mg stretched in the atomic H environment was different. The initial relative activities of Prism I- $\{10\overline{1}0\}$  with H and Basal- $\{0001\}$  with H were 0.605 and 0.395, respectively. The tendency of  $\{10\overline{1}0\}$  of Mg deformed in atomic H was suddenly increased and then slowly decreased, the relative activity of  $\{10\overline{1}0\}$  in atomic H was always lower than that in air. This result was consistent with the calculated  $\gamma_{gsf}$  change in  $\{10\overline{1}0\}[2\overline{1}\overline{1}3]$  whose  $\gamma_{usf}$  improved by 4.5 %. As for  $\{0001\}$  in atomic H environment, its relative activity was reversely decreased with strain applied, but it was 4.6 % higher than that of Mg in air. When the CPFEM was simulated in three dimensions, the difference of relative activity of Basal- $\{0001\}$  was more obvious, which was improved by 26.54 % compared with the  $\{0001\}$  in the 3D Mg-air model (Fig. A.13a).

The volume fraction of twining ( $V_{twin}$ ) was compared in Fig. 14b to show the difference of Mg stretched in air/H environments. It could be found that the  $V_{twin}$  in atomic H was always higher than that of Mg deformed in the air during the whole deformation, and their gap was continuously increasing. Overall, the  $V_{twin}$  of Mg in air/atomic H were both lower than 1.8 %, this was attributed to the small grains and ultra-low strain rate. To further analyze the twin growth rate difference, the  $dV_{twin}/d\delta$  was calculated and summarized in Fig. 14c. During whole deformation, the twin growth rate of Mg stretched in atomic H was greater than that of Mg deformed in air. For the highest twin growth rates, that of Mg in air and atomic H were 17.20 ( $\epsilon$  is 4.73 %) and 19.89 ( $\epsilon$  is 3.00 %), respectively. It

**Table 2**The critical fracture toughness of Mg with H.

Crystal	{0001}	{0001}-H	$\{10\overline{1}0\}$	{1010}−2H	{10 <del>1</del> 0}−6H
$K_{Ic}$ (MPa $\sqrt{m}$ )	0.1647	0.1648	0.2312	0.2229	0.2460

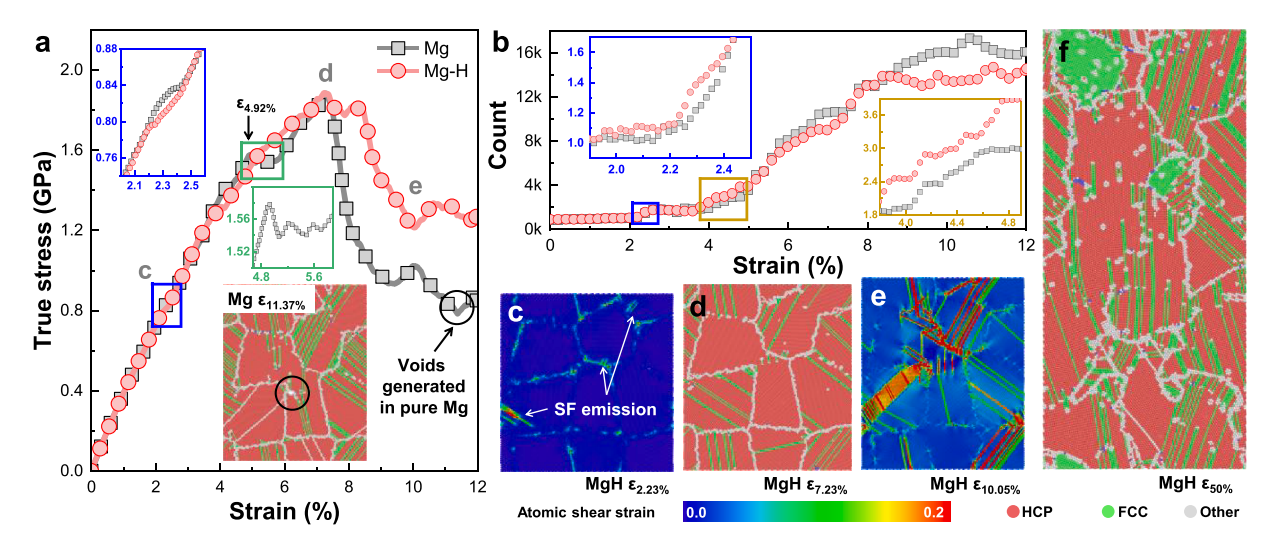


Fig. 12. Tensile simulation of polycrystal Mg with/without H: (a) true stress-strain curve; (b) the number of Mg atoms identified as SF; (c-f) the morphologies of Mg-H model with different strains.

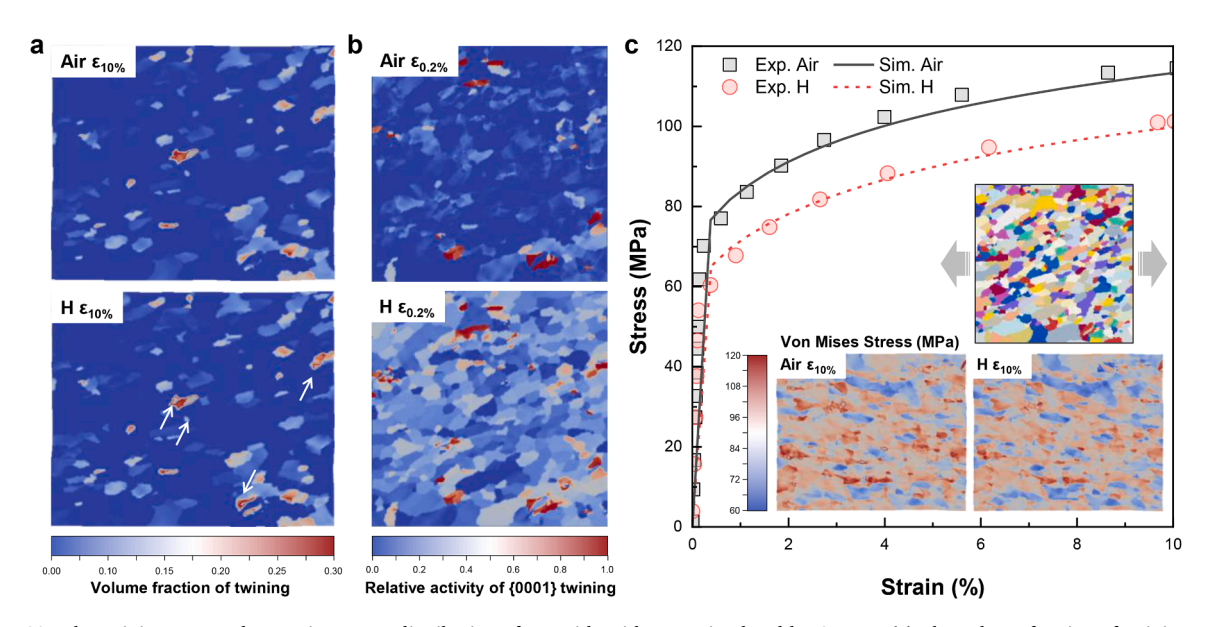


Fig. 13. The twining map and von Mises stress distribution of Mg with/without H simulated by CPFEM: (a) The volume fraction of twining at a strain of 10 %; (b) Relative activity of {0001} twining at a strain of 0.2 %; (c) Comparison of the experimental and simulated strain-stress curve and its von Mises stress distribution at a strain of 10 %.

demonstrated that the Mg stretched in atomic H could generate twins quickly (by  $\sim$ 1.73 % strain in advance). However, the strain with the largest difference in twin growth rate (Fig. 14c blue) was 0.67 %, reaching 7.39. Subsequently, the twin growth rate between Mg deformed in air and atomic H decreased. Differently, the  $V_{twin}$  simulated in the 3D model was lower than that of 2D models, but the atomic H addition still significantly promoted the occurrence of twinning in Mg. The difference of  $V_{twin}$  in the 3D Mg models before/after H permeation was obviously higher than that in 2D models (Fig. A.14b).

According to the relative activity result in Fig. 14a, two grains with different Schmidt factors were selected to compare shear slip (Fig. 15). For  $\{0001\}$  deformation, It could be found that not only the region of Mg in atomic H environment was larger than that in air, but also its highest shear slip (0.113) was greater than that in air (0.107). Differently, the grain with high  $\{10\overline{1}0\} < 2\overline{11}0 > Schmidt factor in atomic H was lower than that deformed in the air, the highest shear slip of Mg in the air was 0.285, while that of Mg in atomic H was only 0.260.$ 

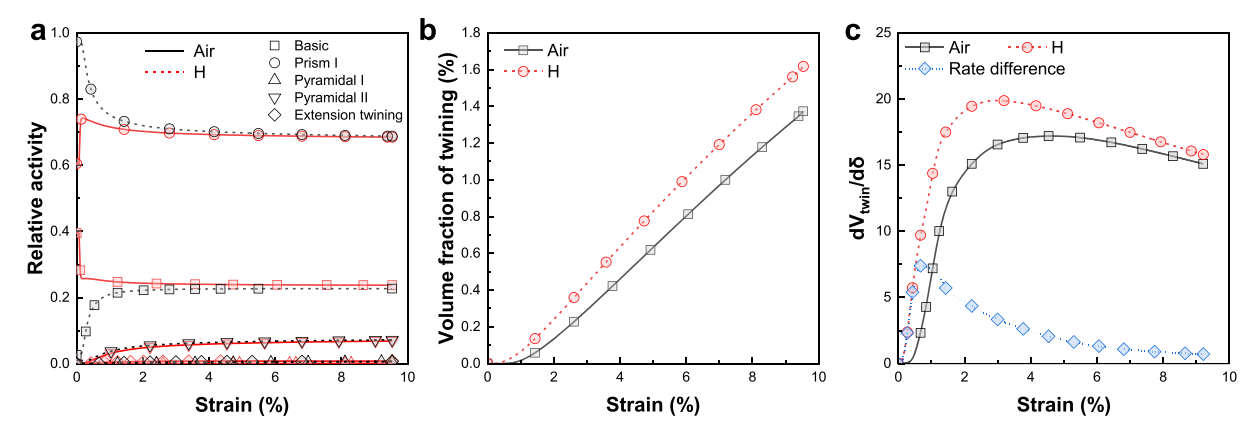


Fig. 14. Relative activity vs equivalent strain for Mg with/without H: (a) Relative activity; (b) Volume fraction of twins; (c) The growth rate difference

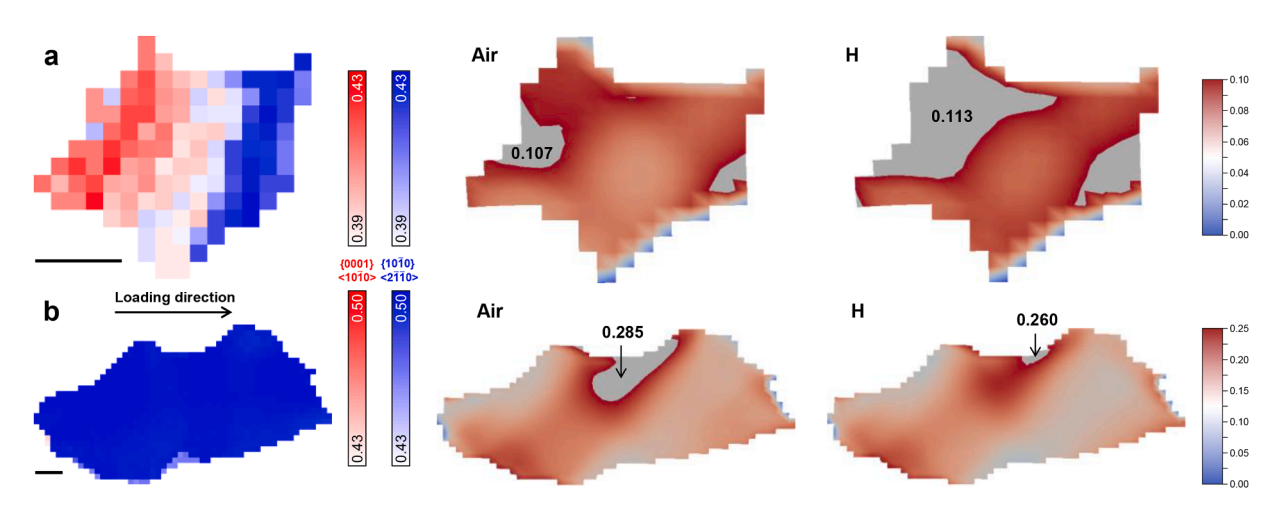


Fig. 15. Comparison of grain deformation on Basal-{0001} and Prism I-{ $10\overline{10}$ }: (a) The grain exhibits high {0001}< $10\overline{10}$ > Schmidt factor; (b) The grain whose { $10\overline{10}$ }< $2\overline{110}$ > Schmidt factor is high. The length scale is 5  $\mu$ m.

#### 4. Discussion

Comprehensively, no Mg surface exhibiting thermodynamic resistance to H, its adsorption or interstitial dissolution is favourable. However, the sensitivity of each orientation to H is different. In terms of surficial effective adsorption site number, the  $\{10\overline{1}0\}$  has the highest density which reaches  $18 \text{ nm}^{-2}$ , while that of  $\{10\overline{1}1\}$  is just  $5 \text{ nm}^{-2}$ . What's worse is that the H diffusion barrier on the  $\{10\overline{1}0\}$  is also the lowest  $(0.156 \text{ eV } H^{-1})$ . It is indicated that there is no resistance to H for  $\{10\overline{1}0\}$ . Although this value is extremely low, whether H can diffuse into the matrix still needs to be determined by combining them with H concentration.

To reduce the Gibbs free energy, molecules diffuse from high to low chemical potential. The Gibbs free energy is affected by the number of molecules in the system. The standard chemical potential  $\mu_0$  ( $\mu_{H0}$ ) represents the Gibbs function of 1 mol of a pure substance (H). The actual chemical potential  $\mu_{Hi}$  of H can be calculated using Eq. (27).

$$\mu_{H_i} = \mu_{H_0} + RT \ln(x_H)$$
 (27)

where R is the gas constant, T indicates the thermodynamic temperature and  $x_H$  represents the mole fraction of H contained in the solution.

According to Lange's Handbook of Chemistry (Dean, 1999), the standard chemical potential of atomic H is  $218 \text{ kJ mol}^{-1}$  and that of  $H^+$  is  $0 \text{ kJ mol}^{-1}$ . Assuming that only  $H^+$  exists in the solution and 298 K, according to Eq. (27), it is inferred that the amount of  $H^+$  reached 1.006 mol. It should be emphasized that the amount of  $H^+$  herein refers to the activity, i.e., the effective concentration of ions participating in the reaction on the surface. However, this H concentration required clearly contradicts the experiment, pure  $H^+$  cannot enter the matrix through the surface. This is because the grains in practice are relatively small, and it is also difficult to concentrate such high  $H^+$  on a specific orientation. Therefore, not diffusing into the matrix, the  $H^+$  mainly undergoes chemical reactions on the

surface which oxidize Mg to  $Mg^{2+}$  and then form the MgH<sub>2</sub>. Unlike the energy required by H diffusion into the matrix, this process is thermodynamically spontaneous, and the formation energy of its products is -0.278 eV atom<sup>-1</sup>.

To confirm the difficulty of dissociating one Mg from surfaces, their  $\Delta G_{dis}$  are computed (Table 3). The results show that the adsorption of H on all orientations can significantly lower the  $\Delta G_{dis}$ . Unfortunately, the H resistance of  $\{10\overline{1}0\}$  is weakest, regardless of the site number, diffusion barrier, and free energy change. Although the  $\Delta G_{dis}$  of the  $\{10\overline{1}1\}$  is also negative, it is protected by the fewest active sites on its surface, and its diffusion barrier is also greater than 0.42 eV. It is worth noting that the  $\{0001\}$  exhibits excellent corrosion resistance. Despite being adsorbed by H, depriving an Mg from  $\{0001\}$  still requires the system to provide 1.77 eV of energy. This also fundamentally explains why the  $\{0001\}$  has the lowest corrosion rate measured in the experiment (Wang et al., 2018).

When there is atomic H in the solution, the required H amount drops to only 1, its chemical potential is greatly higher than the diffusion barriers of all orientations. After the H atoms penetrate the crystal, this process does not cause Mg degradation, but greatly reduces the  $\gamma_{gsf}$  and restores the bulk modulus of the twin. Apart from the  $\{10\overline{10}\}$ , all the slip planes after H permeated exhibit lower  $\gamma_{gsf}$ . Especially for the  $\{0001\}$ , its  $\gamma_{ssf}$  reaches -7.13 mJ  $m^{-2}$  which is lower than the initial structure (HCP, Fig. 9). Importantly, these H atoms should diffuse into the grains (GBs which will be discussed below), so significant H-induced ductility enhancement is observed (Fig. 2). Combined with the EBSD (Fig. 3), it can be found that the length of twins generated with atomic H is twice that in air.

In addition to the SF promotion, the H permeation also significantly affects the propagation of cracking. From the MD/MS simulations, the most important role of H for cracking is to optimize the cleavage cracking of the  $\{0001\}$ , which changes its propagation direction and then emits dislocations. For other orientations, the effect of fewer H atoms will promote the SF emitted earlier, and more H atoms will improve the  $K_{Ic}$ . For the polycrystal Mg model, H also improves the ductility of models, while the H-free model appears voids at a strain of 11.37 %.

It should be noted that to ensure the confinement of H atoms within the grains, the employed temperature is  $\sim$ 0 K. We also simulate the polycrystal Mg model with/without H at 300 K, but the results are obviously reversed. At 300 K, it is difficult to distinguish the effect of H addition on mechanical properties (Fig. 16a), about 49.15 % of H atoms diffuse to GBs. Their ability to promote the occurrence of SF is weakened, while it promotes the generation of large-sized twins (Fig. 16c MgH at a strain of 24.00 %). Under the same concentration of H ( $\sim$ 200 ppm), the polycrystal Mg initiates a crack along GB when the strain reaches 24.00 % (Fig. 16c). However, the model without H has no cracks from the beginning to the end ( $\sim$ 50 % strained). Combined with the high diffusion coefficient ( $\sim$ 10<sup>-9</sup> m<sup>2</sup> s<sup>-1</sup>, 300 K) and strong dissolved site at the GBs ( $\sim$ 1.061 eV  $\sim$ 10<sup>-1</sup>, significantly lower than that inside the grains), H is firmly captured by the GBs (Klyukin et al., 2015; Leitner et al., 2022). Admittedly, there is a shortcoming of polycrystal MD/MS Mg models is that their grain size is only 7.50 $\sim$ 0.56 nm, thereby the H diffusion distance to GBs is relatively short. It is also experimentally confirmed that void nucleation can occur at lower stresses at GBs (Azghandi et al., 2020). In other words, for Mg with tiny grains or undergoing severe deformation (grain breakage caused by rolling), the promotion effect of H on ductility may not be obvious. It explains the reason why the ductility enhancement of pure Mg is apparently weakened than AZ31 Mg alloy to some extent. Fig. 17

For the ductility enhancement problem of the Mg-H system, we combine the DFT calculation, MD/MS simulation, and CPFEM modeling to conduct in-depth computation and analysis. Further attempts are made to link the three methods. For the DFT calculation, it deeply reflects the atomic adsorption/diffusion stable sites and their energy change. Besides, it provides rich force, energy, and stress information that can be used in MD potential training. Although the MD potential used in this study is not trained based on our own DFT dataset, this link is still clear recently (Ji et al., 2024). Meanwhile, MD simulation has the approximate DFT accuracy, it includes the temperature and grains/GB information, reflecting the crack propagation and dislocation emission. This is difficult for both DFT and CPFEM. For the CPFEM modeling, we combine the DFT calculated parameters and experimental fitting parameters, which makes up for the shortcomings of the conventional CPFEM-based trial-and-error method to fit parameters. Sometimes for the same systems, the parameters fitted by this method are not uniform, which cannot reflect the real physical mechanism. However, based on DFT and MD/MS, it can be better elaborated and has proved good applicability in the MgH system.

#### 5. Conclusions

In summary, the elongation and twining of Mg in air and atomic H environments were investigated experimentally. The underlying mechanisms of ductility are comprehensively elucidated using multiscale computations including DFT, MD/MS, and CPFEM. The conclusions are as follows:

(1) Compared with stretched in air, the elongation of the Mg in the atomic H environment is improved by 2.60 %. Deformation promotes the occurrence of Mg twins, but the addition of H increases the number of twins by 167 % compared to Mg strained in air.

**Table 3**The Mg dissociation energy of different orientations.

$\Delta G_{dis}$ (kJ mol <sup>-1</sup> )	{0001}	$\{10\overline{1}0\}$	{10 <u>1</u> 1}
Ideal surface	257.51	-81.54	-56.55
H adsorbed	171.24	-171.53	-153.59

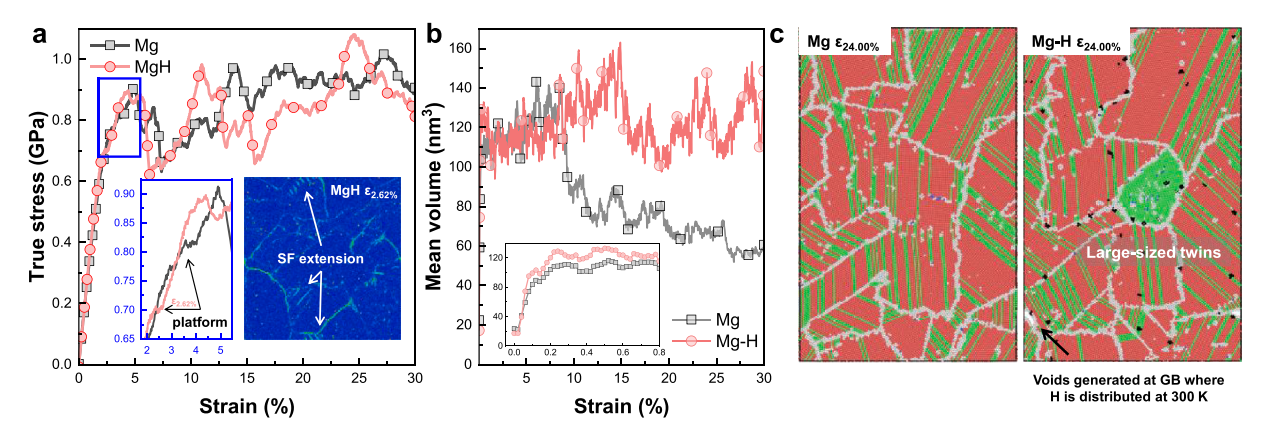


**Fig. 16.** The stress-strain curve and twin volume of Mg with/without H at 300 K: (a) The true stress-strain curve; (b) The volume change of SF with strain; (c) The morphology of Mg with/without H at a strain of 24 %. The black regions are the H-affected atoms.

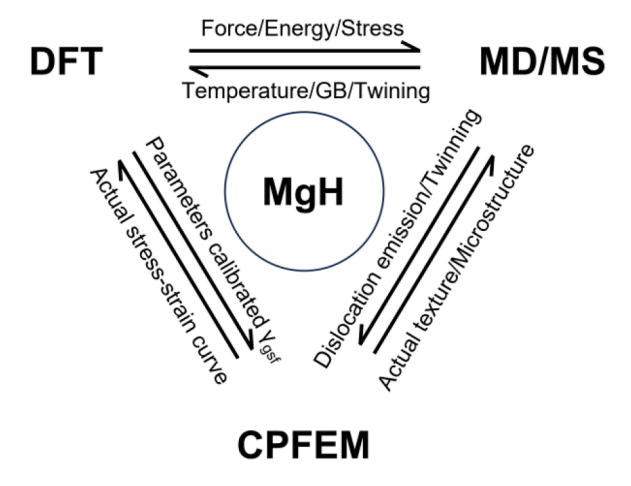


Fig. 17. Multi-scale calculations illustrate the effects of H atoms in Mg from adsorption to penetration, dislocation emission, twinning, crack propagation, and multi-grain deformation.

- (2) The  $\{10\overline{1}0\}$  orientation has the most effective H adsorption sites (18 nm<sup>-2</sup>) and lowest diffusion barrier (0.156 eV  $H^{-1}$ ). Moreover, these properties of  $\{0001\}$  are only 11 nm<sup>-2</sup> and 0.424 eV  $H^{-1}$  respectively. Combined with its Mg dissociation energy (171.24 kJ mol<sup>-1</sup>), the  $\{0001\}$  exhibits the best H resistance.
- (3) The ductility enhancement is attributed to the twinning promoted by H. Except for the  $\{10\overline{1}0\}$ , the generalized stacking fault energy of most orientations is decreased. Especially the  $\{0001\}$ , its  $\gamma_{usf}$  after H permeated is reduced by 18.5 %, reaching 72.3 mJ  $m^{-2}$  and the  $\gamma_{ssf}$  is only -7.13 mJ  $m^{-2}$ . Besides, the permeation of H also impedes the cleavage cracks on the  $\{0001\}$  orientation.
- (4) For polycrystal Mg, the H inside the grains initiates the stacking fault emission earlier, and it can avoid the formation of voids under large strain (50 %). However, once the H atoms are distributed at the GBs, it will lead to rapid failure along the GBs.
- (5) Based on actual grain structure, CPFEM modeling reveals that the Mg strained in atomic H environment exhibits a higher twining volume fraction (17.8 %) than that strained in air. This twin growth difference is mainly concentrated in the first 4 % strain, and there is no obvious difference in the relative activity of plane slip after the 4 % strain.
- (6) As a key intermediate, DFT collaborates with the MD (H sensitive positions) and CPFEM (slip-related generalized stacking fault energy) methods to better elucidate the plastic deformation of Mg in H environments. It both compensates for the inability of traditional CPFEM to explain dislocation emission and crack propagation, and improves the shortcoming that the stress-strain curve simulated by nano-grain MD is greatly different from the actual system.

#### CRediT authorship contribution statement

Yucheng Ji: Writing – original draft, Visualization, Validation, Software, Methodology, Investigation, Formal analysis, Data curation, Conceptualization. Fei Shuang: Methodology. Zhiyang Ni: Methodology, Data curation. Chenyang Yao: Data curation. Xiao Li: Data curation. Xiaoqian Fu: Formal analysis, Data curation. Zhanghua Chen: Conceptualization. Xiaoqang Li: Funding

acquisition. Chaofang Dong: Project administration, Investigation, Conceptualization.

#### Declaration of competing interest

The authors declare that they have no known competing financial interests or personal relationships that could have appeared to influence the work reported in this paper.

#### Data availability

Data will be made available on request.

#### Acknowledgments

This work was supported by the National Natural Science Foundation of China (No.52125102), the China Postdoctoral Science Foundation (No. 2024M750172), Fundamental Research Funds for the Central Universities (No. FRF-TP-20–01B2), Guangdong Basic and Applied Basic Research Foundation (No. 2020B1515120093). Yucheng Ji thanks for the support from the China Scholarship Council (#202106460037). The authors acknowledge the platform support of the National Supercomputer Center in Tianjin and USTB MatCom of Beijing Advanced Innovation Center for Materials Genome Engineering.

#### Supplementary materials

Supplementary material associated with this article can be found, in the online version, at doi:10.1016/j.ijplas.2024.104084.

#### References

Ajito, S., Hojo, T., Koyama, M., Hiromoto, S., Akiyama, E., 2023. Environment-assisted cracking of AZ31 magnesium alloy in a borate buffer solution containing ammonium thiocyanate under various potentials. Corros. Sci. 218, 111195.

Andric, P., Curtin, W., 2018. New theory for crack-tip twinning in fcc metals. J. Mech. Phys. Solids 113, 144–161.

Azghandi, S.M., Weiss, M., Arhatari, B., Adrien, J., Maire, E., Barnett, M., 2020. A rationale for the influence of grain size on failure of magnesium alloy AZ31: an *in situ* X-ray microtomography study. Acta Mater. 200, 619–631.

Baldi, A., Gonzalez-Silveira, M., Palmisano, V., Dam, B., Griessen, R., 2009. Destabilization of the Mg-H System through Elastic Constraints. Phys. Rev. Lett. 102, 226102.

Calado, L.M., Taryba, M.G., Morozov, Y., Carmezim, M.J., Montemor, M.F., 2020. Novel smart and self-healing cerium phosphate-based corrosion inhibitor for AZ31 magnesium alloy. Corros. Sci. 170, 108648.

Chen, Y.S., Huang, C., Liu, P.Y., Yen, H.W., Niu, R., Burr, P., Moore, K.L., Martínez-Pañeda, E., Atrens, A., Cairney, J.M., 2024. Hydrogen trapping and embrittlement in metals–A review. Int. J. Hydrog. Energy.

Chino, Y., Nishihara, D., Ueda, T., Mabuchi, M., 2011. Effects of hydrogen on the mechanical properties of pure magnesium. Mater. Trans. 52, 1123–1126.

Cotterill, P., 1961. The hydrogen embrittlement of metals. Prog. Mater Sci. 9, 205-301.

Dean J.A., 1999. Lange's handbook of chemistry.

Depover, T., Wan, D., Wang, D., Barnoush, A., Verbeken, K., 2020. The effect of hydrogen on the crack initiation site of TRIP-assisted steels during *in-situ* hydrogen plasma micro-tensile testing: leading to an improved ductility? Mater. Charact. 167, 110493.

Fernández, A., Prado, M.T.P., Wei, Y., Jérusalem, A., 2011. Continuum modeling of the response of a Mg alloy AZ31 rolled sheet during uniaxial deformation. Int. J. Plast. 27, 1739–1757.

Gao, Y., Zhao, L., Zha, M., Du, C.F., Hua, Z.M., Guan, K., Wang, H.Y., 2023. Twinning-induced plasticity with multiple twinning modes and disclinations in Mg alloys. Int. J. Plast. 164, 103595.

Gerashi, E., Alizadeh, R., Langdon, T.G., 2022. Effect of crystallographic texture and twinning on the corrosion behavior of Mg alloys: a review. J. Magnes. Alloy 10, 313–325.

Groeber, M.A., Jackson, M.A., 2014. DREAM. 3D: a digital representation environment for the analysis of microstructure in 3D. Integr. Mater. Manuf. I 3, 56–72. He, Y., Peng, C., Feng, Y., Wang, R., Zhong, J., 2020. Effects of alloying elements on the microstructure and corrosion behavior of Mg–Li–Al–Y alloys. J. Alloys Compd. 834, 154344.

Herrera-Solaz, V., LLorca, J., Dogan, E., Karaman, I., Segurado, J., 2014. An inverse optimization strategy to determine single crystal mechanical behavior from polycrystal tests: application to AZ31 Mg alloy. Int. J. Plast. 57, 1–15.

Hill, R., 1952. The elastic behaviour of a crystalline aggregate. Proc. Phys. Soc. A 65, 349.

Hirel, P., 2015. Atomsk: a tool for manipulating and converting atomic data files. Comput. Phys. Commun. 197, 212-219.

Huang, J., Song, G.L., Atrens, A., Dargusch, M., 2020. What activates the Mg surface—A comparison of Mg dissolution mechanisms. J. Mater. Sci. Technol. 57, 204–220.

Ji, Y., Dong, C., Chen, L., Xiao, K., Li, X., 2021. High-throughput computing for screening the potential alloying elements of a 7xxx aluminum alloy for increasing the alloy resistance to stress corrosion cracking. Corros. Sci. 183, 109304.

Ji, Y., Dong, C., Wei, X., Wang, S., Chen, Z., Li, X., 2019. Discontinuous model combined with an atomic mechanism simulates the precipitated  $\eta'$  phase effect in intergranular cracking of 7-series aluminum alloys. Comput. Mater. Sci. 166, 282–292.

Ji, Y., Fu, X., Ding, F., Xu, Y., He, Y., Ao, M., Xiao, F., Chen, D., Dey, P., Qin, W., Xiao, K., Ren, J., Kong, D., Li, X., Dong, C., 2024. Artificial intelligence combined with high-throughput calculations to improve the corrosion resistance of AlMgZn alloy. Corros. Sci. 233, 112062.

Jiang, L., Gong, M., Wang, J., Pan, Z., Wang, X., Zhang, D., Wang, Y.M., Ciston, J., Minor, A.M., Xu, M., Pan, X., Rupert, T.J., Mahajan, S., Lavernia, E.J., Beyerlein, I. J., Schoenung, J.M., 2022. Visualization and validation of twin nucleation and early-stage growth in magnesium. Nat. Commun. 13, 20.

Kalidindi, S.R., 1998. Incorporation of deformation twinning in crystal plasticity models. J. Mech. Phys. Solids 46, 267-290.

Kamilyan, M., Silverstein, R., Eliezer, D., 2017. Hydrogen trapping and hydrogen embrittlement of Mg alloys. J. Mater. Sci. 52, 11091-11100.

Klyukin, K., Shelyapina, M.G., Fruchart, D., 2015. DFT calculations of hydrogen diffusion and phase transformations in magnesium. J. Alloys Compd. 644, 371–377.

- Kresse, G., Furthmüller, J., 1996. Efficiency of ab-initio total energy calculations for metals and semiconductors using a plane-wave basis set. Comput. Mater. Sci. 6, 15–50
- Kumar, P., Ludhwani, M.M., Das, S., Gavini, V., Kanjarla, A., Adlakha, I., 2023. Effect of hydrogen on plasticity of α-Fe: a multi-scale assessment. Int. J. Plast. 165, 103613.
- Lee, C.S., Lee, H.C., Kim, G.h., Han, J.H., Kim, W.J., Kim, H.S., 2019. Design of Mg-6wt%Al alloy with high toughness and corrosion resistance prepared by mechanical alloying and spark plasma sintering. Mater. Charact. 158, 109995.
- Leitner, S., Ecker, W., Fischer, F.D., Svoboda, J., 2022. Thermodynamic trapping and diffusion model for multiple species in systems with multiple sorts of traps. Acta Mater. 233, 117940.
- Li, X.Y., Guo, Y.F., Mao, Y., Tang, X.Z., 2022. Nucleation and growth of {101-1} compression twin in Mg single crystals. Int. J. Plast. 158, 103437.
- Li, Y., Li, W., Min, N., Liu, H., Jin, X., 2020. Homogeneous elasto-plastic deformation and improved strain compatibility between austenite and ferrite in a coprecipitation hardened medium Mn steel with enhanced hydrogen embrittlement resistance. Int. J. Plast. 133, 102805.
- Liu, M., Guo, Y., Wang, J., Yergin, M., 2018. Corrosion avoidance in lightweight materials for automotive applications. npj Mater. Degrad. 2, 24.
- Liu, X., Yin, S., Lan, Q., Xue, J., Le, Q., Zhang, Z., 2017. Investigation of the hydrogen states in magnesium alloys and their effects on mechanical properties. Mater. Des. 134, 446–454.
- Man, C., Dong, C., Wang, L., Kong, D., Li, X., 2020. Long-term corrosion kinetics and mechanism of magnesium alloy AZ31 exposed to a dry tropical desert environment. Corros. Sci. 163, 108274.

#### Michler T., 2010. Hydrogen-induced ductility in aluminum and magnesium alloys. United State Patent, No. 8292206B8292202.

- Nishida, H., Ogawa, Y., Tsuzaki, K., 2022. Chemical composition dependence of the strength and ductility enhancement by solute hydrogen in Fe-Cr-Ni-based austenitic alloys. Mater. Sci. Eng. A 836, 142681.
- Ogawa, Y., Hosoi, H., Tsuzaki, K., Redarce, T., Takakuwa, O., Matsunaga, H., 2020. Hydrogen, as an alloying element, enables a greater strength-ductility balance in an Fe-Cr-Ni-based, stable austenitic stainless steel. Acta Mater. 199, 181–192.
- Sahoo, S.K., Biswas, S., Toth, L.S., Gautam, P.C., Beausir, B., 2020. Strain hardening, twinning and texture evolution in magnesium alloy using the all twin variant polycrystal modelling approach. Int. J. Plast. 128, 102660.
- Salleh, S., Thomas, S., Yuwono, J., Venkatesan, K., Birbilis, N., 2015. Enhanced hydrogen evolution on Mg (OH) 2 covered Mg surfaces. Electrochim. Acta 161, 144–152.
- Sedaghat, O., Abdolvand, H., 2021. A non-local crystal plasticity constitutive model for hexagonal close-packed polycrystals. Int. J. Plast. 136, 102883.
- Sedighiani, K., Diehl, M., Traka, K., Roters, F., Sietsma, J., Raabe, D., 2020. An efficient and robust approach to determine material parameters of crystal plasticity constitutive laws from macro-scale stress-strain curves. Int. J. Plast. 134, 102779.
- Sheppard, D., Xiao, P., Chemelewski, W., Johnson, D.D., Henkelman, G., 2012. A generalized solid-state nudged elastic band method. J. Chem. Phys. 136, 074103. Singh, V., Kumar, R., Charles, Y., Mahajan, D.K., 2022. Coupled diffusion-mechanics framework for simulating hydrogen assisted deformation and failure behavior of metals. Int. J. Plast. 157, 103392.
- Smirnova, D.E., Starikov, S.V., Vlasova, A.M., 2018. New interatomic potential for simulation of pure magnesium and magnesium hydrides. Comput. Mater. Sci. 154, 295–302.
- Song, G.L., Unocic, K.A., 2015. The anodic surface film and hydrogen evolution on Mg. Corros. Sci. 98, 758-765.
- Sprunger, P., Plummer, E., 1991. An experimental study of the interaction of hydrogen with the Mg (0001) surface. Chem. Phys. Lett. 187, 559-564.
- Stampella, R., Procter, R., Ashworth, V., 1984. Environmentally-induced cracking of magnesium. Corros. Sci. 24, 325-341.
- Sun, B., Lu, W., Gault, B., Ding, R., Makineni, S.K., Wan, D., Wu, C.H., Chen, H., Ponge, D., Raabe, D., 2021. Chemical heterogeneity enhances hydrogen resistance in high-strength steels. Nat. Mater. 20, 1629–1634.
- Thekkepat, K., Han, H.S., Choi, J.W., Lee, S.C., Yoon, E.S., Li, G., Seok, H.K., Kim, Y.C., Kim, J.H., Cha, P.R., 2021. Computational design of Mg alloys with minimal galvanic corrosion. J. Magnes. Alloy 10, 1972–1980.
- Tran, R., Xu, Z., Radhakrishnan, B., Winston, D., Sun, W., Persson, K.A., Ong, S.P., 2016. Surface energies of elemental crystals. Sci. Data 3, 1–13.
- Tsakiris, V., Tardei, C., Clicinschi, F.M., 2021. Biodegradable Mg alloys for orthopedic implants A review. J. Magnes. Alloy 9, 1884–1905.
- Wang, N., Mu, Y., Xiong, W., Zhang, J., Li, Q., Shi, Z., 2018. Effect of crystallographic orientation on the discharge and corrosion behaviour of AP65 magnesium alloy anodes. Corros. Sci. 144, 107–126.
- Wang, S., Wang, Y., Ramasse, Q., Fan, Z., 2020. The nature of native MgO in Mg and its alloys. Metall. Mater. Trans. A 51, 2957-2974.
- Wang, Y., Xie, T., Tang, Q., Wang, M., Ying, T., Zhu, H., Zeng, X., 2022. High-throughput calculations combining machine learning to investigate the corrosion properties of binary Mg alloys. J. Magnes. Alloy 12, 1406–1418.
- Wei, J., Li, B., Jing, L., Tian, N., Zhao, X., Zhang, J., 2020. Efficient protection of Mg alloy enabled by combination of a conventional anti-corrosion coating and a superamphiphobic coating. Chem. Eng. J. 390, 124562.
- Wu, L., Cheng, Y., Linghu, F., Jiang, F., Chen, G., Teng, J., Fu, D., Zhang, H., 2021. Microstructure evolution and corrosion resistance improvement of Mg–Gd–Y–Zn–Zr alloys via surface hydrogen treatment. Corros. Sci. 191, 109746.
- Xi, N., Ni, Z., Liu, P., Zhou, Y., Fang, X., Chen, Z., Huang, K., 2024. Prediction of low-cycle fatigue properties of additive manufactured IN718 by crystal plasticity modelling incorporating effects from crystallographic orientations and defects. Virtual Phys. Prototyp. 19, e2328266.
- Xie, D.G., Wan, L., Shan, Z.W., 2021. Hydrogen enhanced cracking via dynamic formation of grain boundary inside aluminium crystal. Corros. Sci. 183, 109307. Yan, C., Xin, Y., Chen, X.B., Xu, D., Chu, P.K., Liu, C., Guan, B., Huang, X., Liu, Q., 2021. Evading strength-corrosion tradeoff in Mg alloys via dense ultrafine twins. Nat. Commun. 12. 4616.
- Yin, B., Wu, Z., Curtin, W.A., 2017. Comprehensive first-principles study of stable stacking faults in hcp metals. Acta Mater. 123, 223-234.
- Yue, Y., Wang, J., Nie, J.F., 2023. Twin-solute, twin-dislocation and twin-twin interactions in magnesium. J. Magnes. Alloy 11, 3427–3462.
- Zhang, M., Ma, A., Llorca, J., 2023. Simulation of dislocation slip and twin propagation in Mg through coupling crystal plasticity and phase field models. Mech. Mater. 180. 104608.
- Zhao, Y., Shi, L., Ji, X., Li, J., Han, Z., Li, S., Zeng, R., Zhang, F., Wang, Z., 2018. Corrosion resistance and antibacterial properties of polysiloxane modified layer-by-layer assembled self-healing coating on magnesium alloy. J. Colloid Interface Sci. 526, 43–50.